

Ionospheric plasma of comet 67P probed by *Rosetta* at 3 au from the Sun

M. Galand,^{1★} K. L. Héritier,¹ E. Odelstad,² P. Henri,³ T. W. Broiles,⁴ A. J. Allen,¹ K. Altwegg,⁵ A. Beth,¹ J. L. Burch,⁴ C. M. Carr,¹ E. Cupido,¹ A. I. Eriksson,² K.-H. Glassmeier,⁶ F. L. Johansson,² J.-P. Lebreton,³ K. E. Mandt,⁴ H. Nilsson,⁷ I. Richter,⁶ M. Rubin,⁵ L. B. M. Sagnières,¹ S. J. Schwartz,¹ T. Sémon,⁵ C.-Y. Tzou,⁵ X. Vallières,³ E. Vigren² and P. Wurz⁵

¹Department of Physics, Imperial College London, Prince Consort Road, London SW7 2AZ, UK

²Swedish Institute of Space Physics, Ångström Laboratory, Lägerhyddsvägen 1, SE-75121 Uppsala, Sweden

³LPC2E, CNRS, Université d'Orléans, 3A, Avenue de la Recherche Scientifique, F-45071 Orléans Cedex 2, France

⁴Southwest Research Institute, PO Drawer 28510, San Antonio, TX 78228-0510, USA

⁵Physikalisches Institut, University of Bern, Sidlerstrasse 5, CH-3012 Bern, Switzerland

⁶Institut für Geophysik und extraterrestrische Physik, TU Braunschweig, Mendelssohnstr. 3, D-38106 Braunschweig, Germany

⁷Swedish Institute of Space Physics, PO Box 812, SE-981 28 Kiruna, Sweden

Accepted 2016 November 7. Received 2016 November 4; in original form 2016 June 21

ABSTRACT

We propose to identify the main sources of ionization of the plasma in the coma of comet 67P/Churyumov–Gerasimenko at different locations in the coma and to quantify their relative importance, for the first time, for close cometocentric distances (<20 km) and large heliocentric distances (>3 au). The ionospheric model proposed is used as an organizing element of a multi-instrument data set from the *Rosetta* Plasma Consortium (RPC) plasma and particle sensors, from the *Rosetta* Orbiter Spectrometer for Ion and Neutral Analysis and from the Microwave Instrument on the *Rosetta* Orbiter, all on board the ESA/*Rosetta* spacecraft. The calculated ionospheric density driven by *Rosetta* observations is compared to the RPC-Langmuir Probe and RPC-Mutual Impedance Probe electron density. The main cometary plasma sources identified are photoionization of solar extreme ultraviolet (EUV) radiation and energetic electron-impact ionization. Over the northern, summer hemisphere, the solar EUV radiation is found to drive the electron density – with occasional periods when energetic electrons are also significant. Over the southern, winter hemisphere, photoionization alone cannot explain the observed electron density, which reaches sometimes higher values than over the summer hemisphere; electron-impact ionization has to be taken into account. The bulk of the electron population is warm with temperature of the order of 7–10 eV. For increased neutral densities, we show evidence of partial energy degradation of the hot electron energy tail and cooling of the full electron population.

Key words: plasmas – methods: data analysis – Sun: UV radiation – comets: individual: 67P.

1 INTRODUCTION

The ESA/*Rosetta* mission, which is the first mission ever to escort a comet, is providing us with the opportunity to assess *in situ* the development and evolution of a cometary coma (Glassmeier et al. 2007a). After a 10-year journey, the *Rosetta* spacecraft reached comet 67P/Churyumov–Gerasimenko (hereafter 67P; Churyumov & Gerasimenko 1972) in summer 2014. Unlike past comet chasers

that were flybys over in hours, the *Rosetta* spacecraft has been escorting comet 67P and probing its plasma environment since 2014 July from 3.8 au to perihelion at 1.24 au reached in 2015 August, to the post-perihelion phase which brought it to 3.5 au in 2016 September at the end of the mission. *Rosetta* is the first mission to orbit a comet, sampling its coma *in situ* at cometocentric distances as low as 10 km, as in 2014 October. Despite low outgassing activity at large heliocentric distances (>2.5 au), the plasma close to comet 67P (<30 km) is primarily of cometary origin with the composition dominated by water ions (Fuselier et al. 2015; Nilsson et al. 2015a,b; Behar et al. 2016). The ionospheric density follows

* E-mail: m.galand@imperial.ac.uk

an r^{-1} dependence up to 260 km and exhibits semi-diurnal variations (Edberg et al. 2015), correlated with those observed in the total neutral density (Bieler et al. 2015b; Hässig et al. 2015; Mall et al. 2016). Furthermore, the electron temperature has values of the order of 5 eV (Odelstad et al. 2015), which is atypically high for an ionospheric plasma.

Our prime objectives are (1) to identify the main source of ionization of the cometary plasma at large heliocentric distances (3.2 au) over a range of sub-spacecraft latitudes; (2) to assess the relative importance, as sources of ionization, of solar extreme ultraviolet (EUV) radiation and energetic electrons, which can be either originating within the comet (e.g. photoelectrons from the coma) or coming from the space environment (e.g. solar wind); (3) to check whether a simple model can capture the large temporal scale variation in ionospheric density; (4) to estimate whether the cometary plasma undergoes any energy degradation.

For that purpose, we propose an ionospheric model which we use to organize a multi-instrument data set from (1) *Rosetta* Plasma Consortium (RPC) sensors (Carr et al. 2007), including the Ion and Electron Sensor (IES; Burch et al. 2007), the LAngmuir Probe (LAP; Eriksson et al. 2007) and the Mutual Impedance Probe (MIP; Trotignon et al. 2007); (2) *Rosetta* Orbiter Spectrometer for Ion and Neutral Analysis (ROSINA) sensors (Balsiger et al. 2007), including the COmet Pressure Sensor (COPS) and the Double Focusing Mass Spectrometer (DFMS); (3) Microwave Instrument on the *Rosetta* Orbiter (MIRO; Gulkis et al. 2007). Data from RPC-fluxgate MAGnetometer (MAG; Glassmeier et al. 2007b) and the RPC-Ion Composition Analyser (ICA; Nilsson et al. 2007) have also been checked; they provide the magnetic field and further particle context during the analysed days.

We focus on the 2014 October period, as in anticipation to the release of the Philae lander, the *Rosetta* spacecraft came very close to within 10 km from the centre of mass of comet 67P, with the goal of mapping the comet surface (global mapping). This close distance leads to a minimal effect of the solar wind on the cometary plasma and the opportunity to be as close as possible to the photoionization source whose associated plasma production occurs in the first few km from the surface (see Section 5). So far, the only other study which assessed the source of ionization was recently proposed by Vigren et al. (2016). They focused on 2015 January 09–11, at a cometocentric distance of 28 km and at a heliocentric distance of 2.6 au over the northern, mid-latitude region. They assumed a pure water coma and neglected electron-impact ionization. By comparing the ionospheric model with RPC-LAP and RPC-MIP, they found that solar EUV radiation alone is the prime source of ionization. They also showed one case (2015 January 31) over the Southern hemisphere where the ionospheric model driven by solar EUV radiation alone largely departs from electron density observations. They speculated that the model departure may be due to a change in composition from an H_2O - to a CO_2 -dominated coma yielding higher ionization frequency and lower outflow velocity.

The originality of our study is the inclusion of electron-impact ionization, the consideration of different neutral species in the coma and the close distance of *Rosetta* to the comet. We also selected observation days which cover a large range of sub-spacecraft latitudes, thus enabling us to cover both summer and winter cometary hemispheres. Finally, comparing electron-temperature-dependent RPC-LAP electron density to RPC-MIP electron density used as reference, it is possible to derive constraints on the electron temperature and to contrast the results with the measurements of the high electron energy tail detected by RPC-IES.

The ionospheric model is described in Section 2, while the data set is introduced in Section 3. The approach applied to the ionospheric model combined with the multi-instrument data set is presented in Section 3.1, and the days selected, conditions encountered, and gas, particle and magnetic field context from ROSINA and RPC sensors are described in Section 3.2. Input physical parameters, including the outflow velocity from MIRO, the neutral composition from ROSINA-DFMS, the solar EUV photoionization frequency and the RPC-IES electron-impact frequency, are presented in Sections 3.3, 3.4.1, 3.4.2, 3.4.3, and electron density from RPC-LAP and RPC-MIP used to compare with the model output, in Sections 3.5 and 3.6, respectively. In Section 4.1, the electron density from RPC-LAP is compared to the RPC-MIP density, and constraints on the electron temperature are derived. Comparison of the modelled ionospheric density with the observed electron density from the RPC sensors is presented for the summer hemisphere in Section 4.2.1 and for the winter hemisphere in Section 4.2.2. Some key assumptions made in the ionospheric model are discussed in Section 5 and concluding remarks are summarized in Section 6.

2 IONOSPHERIC MODEL

The ionospheric model is based on the solution of the coupled, continuity equations applied to cometary ions. The equation at a vector position \mathbf{r} and at a time t for the ion species j is given by

$$\frac{\partial n_j(\mathbf{r}, t)}{\partial t} + \nabla \cdot (n_j(\mathbf{r}, t) \mathbf{u}_j(\mathbf{r})) = P_j(\mathbf{r}, t) - L'_j(\mathbf{r}, t) n_j(\mathbf{r}, t), \quad (1)$$

where n_j is the number density of ion species j and \mathbf{u}_j is the bulk ion velocity. On the RHS, the first term refers to the production rate (in $\text{cm}^{-3} \text{s}^{-1}$) of the ion species j through ionization processes or chemical reactions between cometary ions and neutrals, such as protonation and charge exchange. Charge exchange with solar wind particles is negligible at the close distances we consider (Fuselier et al. 2015; Nilsson et al. 2015a,b). The second term refers to the loss rate of the ion species j due to chemical reactions, such as ion-neutral and electron-ion dissociative reactions. The loss frequency L'_j is expressed in s^{-1} .

We assume that (1) the daughter ions travel radially outwards, similarly to their parent neutrals; (2) the ions do not undergo any acceleration; (3) the ion bulk velocity u_j is assumed to be the same for all ions, referred as u_i , of the order of u_n , the bulk velocity for the neutrals and to be independent of r . The validity of these assumptions is discussed in Section 5. We also assume that all physical quantities in equation (1) are only dependent on the radial coordinate r and independent of the polar angle θ and the azimuth angle ϕ .

Thus, equation (1) expressed in spherical, polar coordinates becomes

$$\frac{\partial n_j(r, t)}{\partial t} + \frac{1}{r^2} \frac{\partial}{\partial r} (r^2 n_j(r, t) u_i) = P_j(r, t) - L'_j(r, t) n_j(r, t). \quad (2)$$

At the close cometocentric distances considered in the present study (< 20 km), ions produced near the surface ($r_s = 1.5$ km) take less than a minute (46 s at 400 m s^{-1}) to reach the spacecraft. Over such a time period, the solar flux can be assumed unchanged. We assume that it is also the case for the electron-impact ionization source. In addition, we solved the set of ion continuity equations applied to the conditions encountered at 3 au, following the method of Vigren & Galand (2013). In the model, the time it takes to reach convergence

at cometocentric distances of 20 km or lower is at least two orders of magnitude less than the time it takes for an ion produced near the surface to reach a given cometocentric distance. Hence, we look for steady-state solutions and neglect the first term on the LHS of equation (2) thereafter.

Our ionospheric model solves the coupled, continuity equations (2) and provides the number density for each of the ion species considered, as illustrated in Vigren & Galand (2013), Fuselier et al. (2015, 2016) and Beth et al. (2016). Here it is however worthwhile to derive a simple relation to calculate the total ion density, n_i , referred hereafter as the ionospheric density. Summing the ion continuity equations over all ion species yields

$$\frac{1}{r^2} \frac{d}{dr} (r^2 n_i(r) u_i) = P_i(r) - L_i'(r) n_i(r). \quad (3)$$

P_i is reduced to the production of primary ions, and L_i' , to the net loss of positive charge, that is, the net loss in the total ion population. Indeed, in equation (2) applied to ion species j , the ion production rate associated with the reaction between the neutral species l and the ion species k and producing the ion species j (e.g. $\text{H}_3\text{O}^+ + \text{NH}_3 \rightarrow \text{NH}_4^+ + \text{H}_2\text{O}$) is equal to the loss rate associated with the same reaction, present in the continuity equation of the ion species k . Therefore, when summing all the ion equations together, these ion–neutral terms cancel out.

Ionization sources. Primary cometary ions are produced through EUV photoionization (see Section 3.4.2) and electron-impact ionization (see Section 3.4.3). The total ion production rate is defined as

$$P_i(r) = \sum_l (v_l^{hv}(r) + v_l^e(r)) n_l(r), \quad (4)$$

where v_l^{hv} and v_l^e are the solar EUV and electron-impact ionization frequencies, respectively, of neutral species l and n_l is the number density of the neutral species l . As the atmosphere is optically thin to EUV radiation, v_l^{hv} is independent of r (see Section 3.4.2). Electron-impact frequency v_l^e is derived at the cometocentric distance r_0 of *Rosetta* (see Section 3.4.3). For simplification, we assume that the ionizing electrons ($E > 12$ eV, see Table 2) do not undergo any substantial change in number flux and in energy between *Rosetta* and the surface, that is $v_l^e(r) = v_l^e(r_0)$. The implication of this assumption is discussed in Section 5.

Furthermore, as their cross-sections are very low compared with single ionization cross-sections and as we are focusing on the total ionospheric density, double-ionization processes are ignored. Therefore, the ionization frequency is associated with single ionization cross-section, including both non-dissociative and dissociative ionizations as well as ionization yielding the ion species in an excited state.

Neutral number density. The number density $n_l(r)$ of the neutral parent species l is given by

$$n_l(r) = v_l n_n(r), \quad (5)$$

where v_l is the volume mixing ratio of l and is assumed to be independent of the cometocentric distance r (see Section 3.4.1) and $n_n(r)$ is the total neutral number density. The density $n_n(r)$ measured by ROSINA-COPS was found to follow an r^{-2} dependence over the distances covered by the spacecraft (Bieler et al. 2015b; Hässig et al. 2015). This is consistent with the conservation of the flux, assuming a constant, radial expansion velocity, non-reactive species, and negligible loss through, e.g. photoionization and photodissoci-

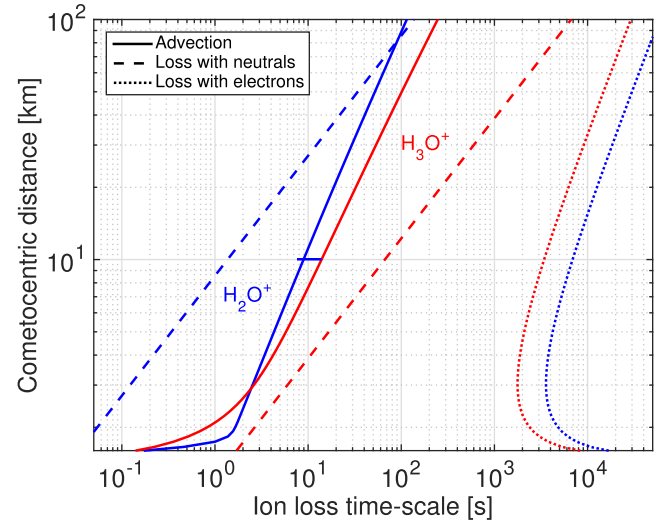


Figure 1. Ion loss time-scales for an activity parameter $\xi = 3 \times 10^{20} \text{ cm}^{-1}$ for the primary ion H_2O^+ (blue lines) and the secondary ion H_3O^+ (red lines). The time-scales for reactions between ions and neutrals ($\text{H}_2\text{O}^+ + \text{H}_2\text{O}$ and $\text{H}_3\text{O}^+ + \text{HPA}$) are shown in dashed lines. The time-scales for the dissociative recombination reactions between ions and electrons are shown in dotted lines. The advection time-scales τ_{adv} are plotted with solid lines for $u_i = 600 \text{ m s}^{-1}$. The horizontal, blue line represents the range of H_2O^+ advection time-scale values at 10 km for u_i varying between 400 and 700 m s^{-1} (see Section 3.3).

ation. As a consequence, we introduce the ‘activity’ parameter ξ to define n_n , as follows:

$$\xi = n_n(r) r^2 = n_n(r_0) r_0^2, \quad (6)$$

where $n_n(r_0)$ is the total number density at the cometocentric distance r_0 of *Rosetta* (see Section 3.1(i)). The parameter ξ , which is directly derived from ROSINA-COPS observation, is a good proxy for the local outgassing activity, though it also depends on the neutral outflow velocity. Departure of n_n from the r^{-2} dependence is discussed in Section 5.

Effective ionization frequencies. We introduce the effective photoionization frequency v^{hv} at a heliocentric distance d_h defined as

$$v^{hv} = \sum_l v_l^{hv} \frac{v_l}{f_c} = \sum_l \frac{v_{l,1\text{au}}^{hv}}{d_h^2} \frac{v_l}{f_c} = \frac{v_{1\text{au}}^{hv}}{d_h^2}, \quad (7)$$

where f_c is the composition correction factor for the ROSINA-COPS neutral density (see Section 3.4.1). $v_{1\text{au}}^{hv}$ is the effective photoionization frequency at 1 au and $v_{l,1\text{au}}^{hv}$ is the photoionization frequency of neutral species l at 1 au, derived in Section 3.4.2. The effective electron-impact ionization frequency $v^e(r_0)$ at r_0 is given by

$$v^e(r_0) = \sum_l v_l^e(r_0) \frac{v_l}{f_c}, \quad (8)$$

where the ionization frequency $v_l^e(r_0)$ is derived in Section 3.4.3.

The total ion production rate P_i is thus given by

$$P_i(r) = (v^{hv} + v^e(r_0)) n_n(r_0) \left(\frac{r_0}{r}\right)^2. \quad (9)$$

Ion loss time-scales. Ion chemical loss and advection time-scales are shown in Fig. 1 for the highest neutral density encountered in the present study (activity parameter $\xi = 3 \times 10^{20} \text{ cm}^{-1}$, see Table 1) and a neutral outflow velocity of 600 m s^{-1} . The volume mixing ratio of water is assumed to be 95 per cent (see Section 3.4.1) and the one of neutral species with a proton affinity higher than the

Table 1. Selected days and associated heliocentric distance d_h , *Rosetta* sub-spacecraft latitude range, mean cometocentric distance \bar{r}_0 over the day and daily maximum of the activity parameter ξ derived from ROSINA-COPS. For 2014 October 18 and 19, the maximum value of ξ corresponds to the Southern hemisphere (SH; including only negative latitudes). The last three columns correspond to the photoionization frequency $\nu_{l,1\text{ au}}^{hv}$ at 1 au in units of (10^{-7} s^{-1}), computed from the daily TIMED/SEE solar spectral flux observed at Earth δ_{Earth} days later the selected day at comet 67P, due to the phase angle ϕ_{Sun} between the Earth, the Sun and comet 67P.

Selected day	d_h (au)	Latitude ($^\circ$)	\bar{r}_0 (km)	max ξ (cm^{-1})	$\phi_{\text{Sun}} (^\circ)$	$\delta_{\text{Earth}} (\text{d})$	$\nu_{\text{H}_2\text{O},1\text{ au}}^{hv}$	$\nu_{\text{CO},1\text{ au}}^{hv}$	$\nu_{\text{CO}_2,1\text{ au}}^{hv}$
2014 Oct 03	3.253	47 to 26	19.0	2.4×10^{20}	-72.6	5	6.78	8.23	11.60
2014 Oct 04	3.247	26 to (-8)	19.0	1.8×10^{20}	-73.5	5	6.67	8.12	11.43
2014 Oct 17	3.164	49 to 19	10.0	3.0×10^{20}	-84.5	6	6.93	8.31	11.99
2014 Oct 18	3.158	19 to (-47)	10.0	7.6×10^{19} (SH)	-85.3	6	6.94	8.31	12.12
2014 Oct 19	3.151	(-47) to 39	9.5–10.0	7.8×10^{19} (SH)	-86.2	6	7.05	8.45	12.35
2014 Oct 20	3.145	50 to (-15)	9.0–9.5	2.6×10^{20}	-87.0	6	7.03	8.42	12.29

Table 2. Parameters used for $n_i(r_0)$ adjustment, β_l (see table 4.4, p. 4.9 in Granville-Phillips 2014), and volume mixing ratio, v_l , for the Northern hemisphere (NH) and the Southern hemisphere (SH) (Le Roy et al. 2015), for the neutral species l included in the ionospheric model. Also given are the ionization threshold energy E_l^{th} and associated wavelength λ_l^{th} for the single, non-dissociative ionization of the neutral species l yielding the ion species in the ground state.

Neutral species l	H ₂ O	CO	CO ₂
β_l	0.893	0.952	0.704
v_l (NH) (per cent)	95	2.6	2.4
v_l (SH) (per cent)	50	10	40
E_l^{th} (eV)	12.6	14.0	13.8
λ_l^{th} (nm)	98	89	90

affinity of water, referred hereafter as high proton affinity (HPA) neutrals, to be 2 per cent, an upper limit (Le Roy et al. 2015).

The advection time-scale $\tau_{\text{adv},j}$ of the ion species j is defined as

$$\frac{1}{\tau_{\text{adv},j}} = \frac{1}{r^2 n_j(r)} \frac{d(r^2 n_j(r) u_i)}{dr} = \frac{1}{\tau_g} - \frac{1}{\tau_{n_j}}. \quad (10)$$

The time-scale $\tau_g = (\frac{u_i}{r^2} \frac{dr^2}{dr})^{-1} = (\frac{r}{2u_i})$ represents the geometric time-scale associated with the spherical symmetry and independent of the ion species considered. The time-scale $\tau_{n_j} = -(\frac{u_i}{n_j(r)} \frac{dn_j(r)}{dr})^{-1}$ represents the ion density gradient time-scale. It is dominant and negative very close to the surface ($r < 1\text{--}2$ km) and positive above. The sensitivity of the advection time-scale to u_n ranging from 400 to 700 m s⁻¹ (see Section 3.3) is shown with a horizontal bar. The primary ion considered is H₂O⁺, which can be lost through protonation of water to produce the secondary ion, H₃O⁺. The latter could be similarly lost through protonation of HPA neutral species (e.g. NH₃ producing NH₄⁺; Allen et al. 1987; Vigren & Galand 2013; Beth et al. 2016). The values for the reaction rates ‘ion + neutral’ and ‘ion + e-’ are from Vigren & Galand (2013). The electron temperature is taken to be 200 K (≈ 0.02 eV) to provide the lowest possible values for the electron-ion recombination time-scales. This temperature corresponds to a typical value of the surface temperature derived on the dayside from VIRTIS (Visible, Infrared and Thermal Imaging Spectrometer; Capaccioni et al. 2015). It is significantly less than what is observed at the location of *Rosetta* (> 5 eV), which yields recombination time-scales two orders of magnitude higher with a minimum of the order of 10^5 s, but closer to the comet more energy degradation occurs for the electrons bringing T_e closer to T_n . Fig. 1 shows that (1) the primary ion H₂O⁺ is efficiently lost by reacting with water (blue dashed line); the associated time-scale has values significantly lower than the advection time-scale (blue solid

line); therefore, advection can be neglected at cometocentric distances below 40 km, while it becomes increasingly important above; (2) the secondary ion H₃O⁺ is dominantly lost through advection (Fuselier et al. 2015); (3) electron-ion dissociative recombination reactions have loss time-scales significantly larger than advection, meaning that the terminal ion species (H₃O⁺ or NH₄⁺) is lost through transport. Chemical loss processes can therefore be neglected when calculating the total ion density. We have considered here the main chemical pathway for the water ions. The same conclusions are reached when considering CO⁺ or CO₂⁺ as primary ions. Furthermore, we have ignored the interaction of the gas with dust grains. At 3 au, dust charging can be neglected for total charge balance, though it may be important near perihelion (Vigren et al. 2015a). Therefore, in the following, total ion number density n_i is assumed to be equal to the electron density n_e .

Combining all these together [including equations (6) and (9)], equation (3) is reduced to

$$d(r^2 n_i(r) u_i) = (v^{hv} + v^e(r_0)) n_n(r_0) r_0^2 dr. \quad (11)$$

Assuming that the ionospheric density is zero at the cometary surface, r_s (taken to be 1.5 km), integrating equation (11) from r_s to r yields this simple relation for the ionospheric density at a cometocentric distance r ($\leq r_0$):

$$n_i(r) = \frac{(v^{hv} + v^e(r_0)) (r - r_s)}{u_i} n_n(r). \quad (12)$$

Equation (12) implies that away from the surface $n_i(r)$ decreases as r^{-1} , which is a consequence of the r^{-2} dependence of $n_n(r)$ [see equations (6) and (9); Bieler et al. 2015b; Hässig et al. 2015]. The difference between the dependence with r in n_n and n_i results from the fact that besides transport from below, there is also an additional source of ions through local photoionization of the cometary neutrals. When chemical loss becomes significant, which requires a higher outgassing rate than experienced by comet 67P at 3 au, the decrease of n_i in r becomes sharper (Vigren & Galand 2013). Note also that from equation (12), ion-to-neutral number density ratio, n_i/n_n , is given by the ionization frequency multiplied by $(r - r_s)/u_i$, that is, multiplied by the time taken by the gas to propagate from the surface to the spacecraft (Vigren et al. 2015b).

3 DATA SET USED

3.1 Organization of the multi-instrument data set

Fig. 2 illustrates how the simplified ionospheric model described in Section 2 is organizing the *in situ* RPC and ROSINA multi-instrument data set measured at the cometocentric distance r_0 of

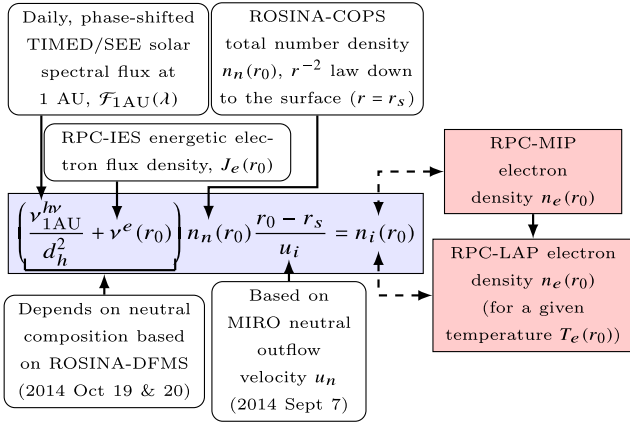


Figure 2. Schematic of the simplified ionospheric model (blue box) and the *Rosetta* multi-instrument data set from RPC and ROSINA sensors at the cometocentric r_0 of *Rosetta* at a given time t . The observations used to calculate the ionospheric density n_i are shown in white boxes and those used to compare directly with the modelled density n_i are shown in red boxes.

Rosetta at a given time t . The physical quantities the model is based on and which vary with time are as follows.

(i) **The total number density** $n_n(r_0) = n_C(r_0) - n_{bg}$, where n_C is the neutral number density measured by ROSINA-COPS nude gauge and n_{bg} is the background number density equal to $1.2 \times 10^6 \text{ cm}^{-3}$ (Schläppi et al. 2010). Its behaviour over latitude and longitude is discussed in Section 3.2. The neutral density $n_n(r_0)$ has not been corrected for the neutral composition. This would require dividing $n_n(r_0)$ by the composition correction factor, f_C , defined in Section 3.4.1. Instead, the factor f_C is included in the effective ionization frequencies – defined in equations (7) and (8) – which are the only composition-dependent parameters in equation (12) defining the ionospheric density n_i .

(ii) **The ion outflow velocity** u_i whose range of considered values are based on the neutral outflow velocity measurements from MIRO (see Section 3.3).

(iii) **The effective photoionization frequency** ν_{1AU}^{hv} derived from the daily solar flux observed at Earth and extrapolated in heliocentric distance (d_h) and in days due to the phase angle between the Earth, the Sun and the comet (see Section 3.4.2).

(iv) **The effective electron-impact ionization frequency** $\nu^e(r_0)$ derived from the energetic electron flux density measured by RPC-IES at r_0 (see Section 3.4.3).

(v) **The neutral composition** based on two sets of measurements from ROSINA-DFMS (see Section 3.4.1). Both effective photoionization and electron-impact ionization frequencies depend on it.

The RPC-LAP (see Section 3.5) and RPC-MIP (see Section 3.6) electron densities are compared with the ionospheric density calculated from equation (12) at the cometocentric distance r_0 of *Rosetta* at time t (see Section 4). The electron temperature T_e of the cometary population is discussed in Section 4.1.

3.2 Overview of the selected days

Table 1 provides a summary of the observation days we have selected for this study. The choice was driven by the cometocentric distance to be less than 20 km, the availability of high-quality data set for at least RPC-LAP or RPC-MIP (for n_e) and of ROSINA-COPS (for n_n). Days were selected over a wide range of sub-spacecraft latitudes to cover both hemispheres. We have selected two periods:

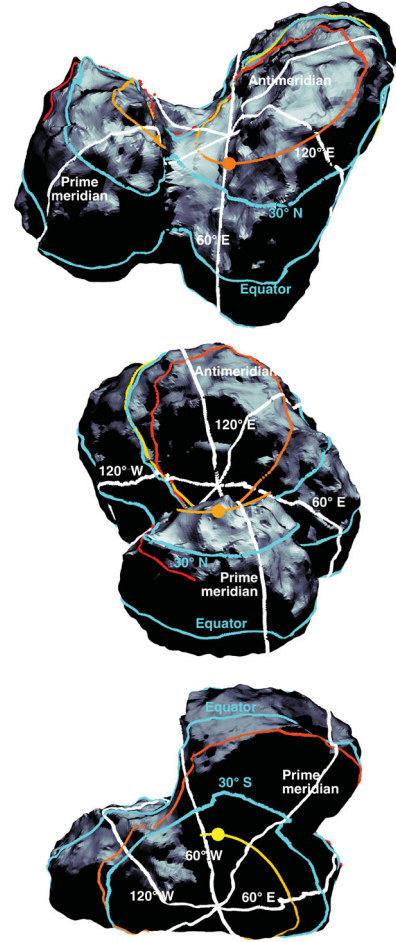


Figure 3. Configuration of comet 67P as seen from *Rosetta*: (top) at 11:46 UT on 2014 October 17 (49°N latitude, 64°E longitude) and (middle) at 15:30 UT on 2014 October 17 (46°N latitude, 16°W longitude) over summer; (bottom) at 23:00 UT on 2014 October 18 (49°S latitude, 43°W longitude) over winter. The trajectory of *Rosetta* is radially projected on the cometary surface for the day of observation from red (00 UT) to yellow (24 UT). The large orange/yellow dots correspond to the sub-spacecraft location at the time identified above. The latitudes and longitudes on comet 67P are shown in cyan and white, respectively. The grey shade on the cometary body corresponds to the solar illumination corrected for a viewing from *Rosetta* (see the text).

2014 October 03–04, with r_0 close to 20 km, and 2014 October 17–20, with r_0 close to 10 km. Over these days, *Rosetta* was in the terminator plane with a phase angle between 89° and 93° and the subsolar latitude was about 40°. During 2014 October 03, 04, 17 and 20, *Rosetta* was primarily over the positive northern, summer latitudes, while during 2014 October 18–19, it made an excursion over the negative southern, winter latitudes.

Fig. 3 illustrates the cometary configuration as seen from *Rosetta* for three extreme cases: over the summer hemisphere during a local maximum in the outgassing rate associated with $\xi = 2.7 \times 10^{20} \text{ cm}^{-1}$ (top panel) and a local minimum associated with $\xi = 5.4 \times 10^{19} \text{ cm}^{-1}$ (middle panel) and over the winter hemisphere with $\xi = 3.8 \times 10^{19} \text{ cm}^{-1}$ (bottom panel). The trajectory is shown from red (00 UT) to yellow (24 UT). Note that due to the degeneracy in the cometary shape, different points on the comet may have the same set of latitude and longitude. The large coloured dot represents the sub-spacecraft radial projection on the cometary surface. The grey shade illustrates the solar illumination, which is defined as the cosine

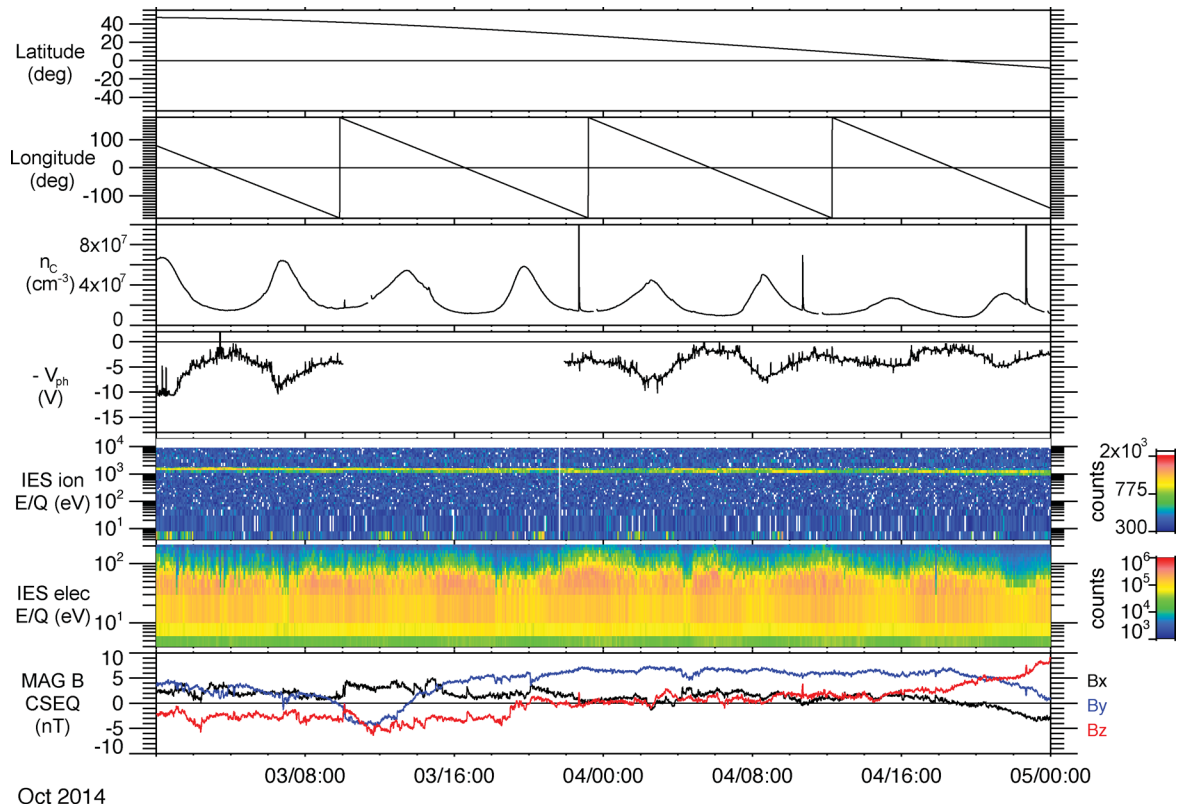


Figure 4. Compilation of the neutral, particle and magnetic field conditions on 2014 October 03 and 04, at 19 km cometocentric distance. From top to bottom panels are shown the time series for the sub-spacecraft latitude and longitude (in $^{\circ}$) of the location of *Rosetta* radially projected on comet 67P, the total number density from ROSINA-COPS $n_c(r_0)$, defined in Section 3.1(i) (in cm^{-3}), the spacecraft-to-Langmuir probe potential from RPC-LAP (in V), the energetic ion and electron spectra from RPC-IES (in raw counts per 45.6 s) and the magnetic field components of the outboard RPC-MAG sensor (in nT) expressed in the CSEQ coordinate system. On October 03, there was no measurement from RPC-LAP between 10 and 22 UT, while RPC-MIP was operating in the LDL mode.

of the ‘Sun–comet–radial direction’ angle multiplied by the cosine of the ‘radial direction–comet–*Rosetta*’ varying from darkness (≤ 0) shown in black to overhead Sun as seen from *Rosetta* ($=1$) shown in white. Outgassing rate varies with geometry and solar illumination: the level of illumination and the viewing area of the comet as seen from *Rosetta* decrease from the top (high ξ) to the bottom (low ξ) panels. This results from diurnal variations (top versus middle panels) and from seasonal change from summer (top and middle panels) to winter (bottom panel).

Figs 4 and 5 provide an overview for 2014 October 03–04 and 2014 October 17–20, respectively, in terms of sub-spacecraft latitude and longitude of *Rosetta* with respect to comet 67P, total neutral number density n_c from ROSINA-COPS (Balsiger et al. 2007), the $(-V_{ph})$ potential from the spacecraft to the Langmuir probe derived from RPC-LAP – where V_{ph} , a positive quantity, represents the photoelectron knee potential – (Odelstad et al. 2015, see also Section 3.5), ion and electron spectra from RPC-IES (Burch et al. 2007), and magnetic field components from RPC-MAG (Glassmeier et al. 2007b) given in the Cometocentric Solar Equatorial (CSEQ) coordinates. In the CSEQ system, the x -axis points towards the Sun, the z -axis is the projection of Sun’s rotational axis perpendicular to the x -axis and the y -axis completes the right-handed system and is therefore close to the Sun’s equatorial plane. RPC-ICA (Nilsson et al. 2007) was not operating over the selected periods, except between 11:30 and 20:30 UT on 2014 October 17 and between 13 and 21 UT on 2014 October 19. This limited data set is not shown in the overview figures but similar data set is presented in Nilsson et al. (2015a,b). The RPC-LAP and RPC-MIP

ionospheric densities are introduced in Sections 3.5 and 3.6 and presented in Section 4.

The ROSINA-COPS total neutral number density $n_c(r_0)$ is shown in the third panel from top in Figs 4 and 5. On 2014 October 19, ROSINA-COPS was off during series of large manoeuvres, which occurred between 07:25 and 12:15 UT. In addition, due to significant spacecraft manoeuvres, including reaction wheel off-loading, outgassing from illuminated spacecraft surfaces previously in the shadow (and on which gas from both the spacecraft and the comet is frozen) is responsible for the sharp peaks seen in n_c at 22:40 UT each day, at 10:40 UT on October 04 and 18, at 10:05 UT on October 17, between 14:30 and 15:30 UT, near 18:30 UT on October 18, and between 10:00 and 11:00 UT and between 14:00 and 15:00 UT on October 20. Also, near 11:55 UT on October 17, near 02:30 UT on October 18 and near 02:10 UT, 06:15 UT and 18:10 UT on October 20, the measurements of n_c have been perturbed by small slews of the spacecraft.

The ROSINA-COPS neutral density varies with both latitudinal (seasonal) and longitudinal (diurnal) conditions, as a result of variations in solar illumination, in surface composition and in topography, confirming previous studies based on the analysis of ROSINA (Hässig et al. 2015; Mall et al. 2016), MIRO (Biver et al. 2015; Gulkis et al. 2015; Lee et al. 2015) and VIRTIS (Bockelée-Morvan et al. 2015) observations. The hemispheric difference in outgassing rates is mainly driven by differences in illumination and geometry (Bieler et al. 2015b, see Fig. 3). In the northern, summer hemisphere, the surface temperature is higher and sublimation of all volatiles, including water, is efficient, compared with the southern, winter

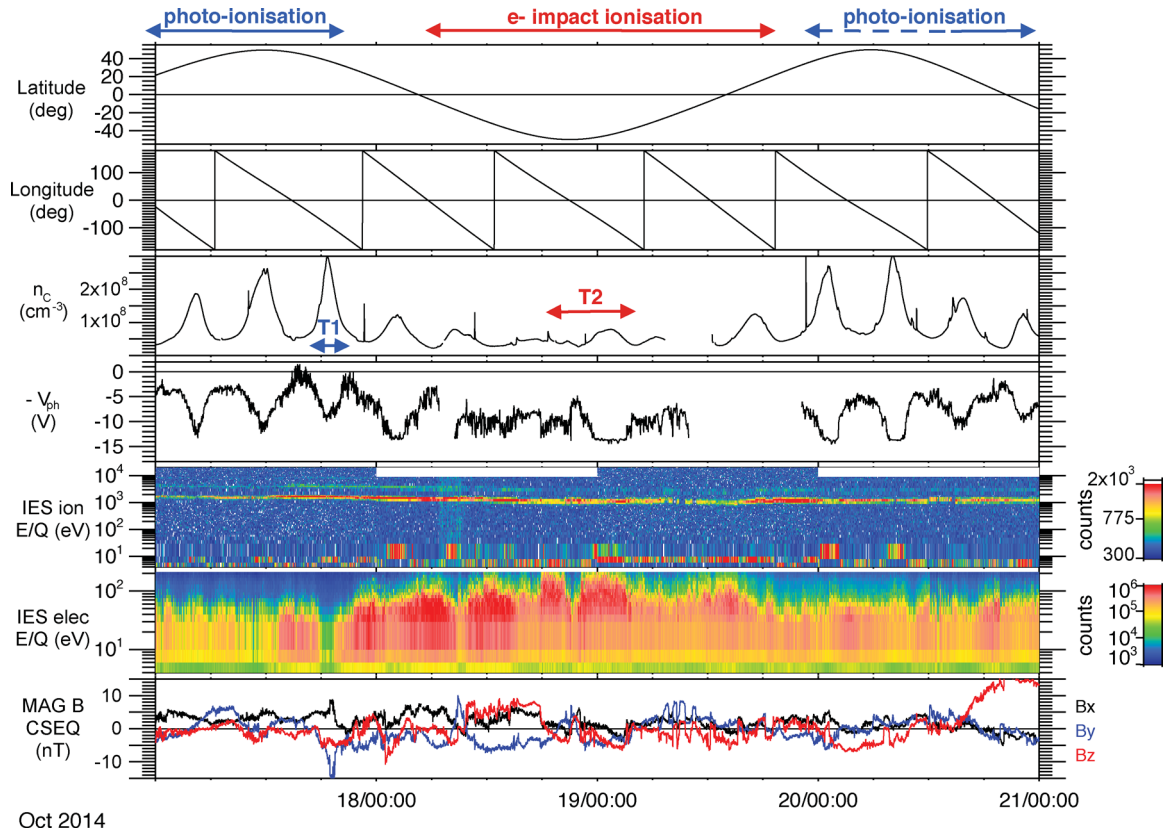


Figure 5. Same as for Fig. 4, but for 2014 October 17–20, at a cometocentric distance of 10 km. On October 19, ROSINA-COPS was switched off during orbital correction manoeuvres from 07:25 to 12:15 UT. There was also no RPC-LAP measurement on October 19 between 10 and 22 UT while RPC-MIP was operating in the LDL mode, and on October 18 between 07:00 and 08:30 UT. The blue arrows represent high neutral density periods during which photoionization is driving the ionospheric densities overall, while the red arrow represents a low neutral density region during which electron-impact ionization is dominant. The regions in between are transition regions over which both ionization processes are significant. The period identified as T1 (extending from 17:30 to 20:00 UT on 2014 October 17, with the maximum near 18:30 UT) corresponds to the strongest neutral density peak over the selected days. The period identified as T2 (extending from 18 UT on 2014 October 18 to 04 UT on 2014 October 19, over the negative mid-latitudes of the winter hemisphere) is associated with a correlation between ROSINA-COPS n_c and RPC-IES electron count rates.

hemisphere with a colder, shadowed surface. Hemispheric differences in the outgassing rate may also result from inhomogeneity in the ice distribution (Bieler et al. 2015b; Capaccioni et al. 2015; Sierks et al. 2015; Fougere et al. 2016). This inhomogeneity might not be primordial: it may be a thermal evolution resulting from the very asymmetric seasonal cycle between the two hemispheres (Le Roy et al. 2015). The most active day in the selected data set is 2014 October 17 (period T1 in Fig. 5 associated with the n_c peak near 18:30 UT), with a maximum value for the activity parameter ξ of $3 \times 10^{20} \text{ cm}^{-1}$. This is almost three times the maximum value of ξ observed over the Southern hemisphere probed only up to mid-latitudes (see Table 1). Besides the latitudinal dependence, the number density n_c also varies with longitude. As *Rosetta* moves very slowly compared with the comet (about 1 m s^{-1}), it sees the comet rotating below it. Over the Northern hemisphere, the comet shows a clear, semi-diurnal variation with a period of 6.2 h, half its rotation period. The maxima correspond to times at which (1) the neck (at $+60^\circ$ and -120° longitude) located between the two lobes is visible from the position of *Rosetta* as it contributes additionally to the default outgassing (Bieler et al. 2015b); (2) a large area of the partially illuminated comet is seen from *Rosetta*, as illustrated in the top panel of Fig. 3. The minima correspond to times during which the total area seen from *Rosetta* is reduced and the neck is hidden as illustrated in the middle panel of Fig. 3. The semi-diurnal

variation seems to be driven by water, which dominates the coma composition over the Northern hemisphere. It disappears over the mid-latitudes of the Southern hemisphere where carbon dioxide, which exhibits a different variation from water, becomes significant (see Section 3.4.1).

The spacecraft is negatively charged during the selected period. The potential ($-V_{ph}$) from the spacecraft to the RPC-LAP probe (fourth panel from top in Figs 4 and 5) is proportional to the true spacecraft potential V_{SC} with respect to infinity (see Section 3.5). There is no potential information from RPC-LAP during the 12 h of operation of RPC-MIP – in the so-called LDL mode, making use of one of the two RPC-LAP probes (see Section 3.6) – on 2014 October 03 and on 2014 October 19. In addition, the RPC-LAP probes were operating in electric field mode between 07:00 and 08:30 UT on 2014 October 18. This mode is not optimum for deriving the spacecraft potential. The sharp, negative values seen on 2014 October 17, between 10 and 17 UT, result from non-physical perturbations. The spacecraft potential is representative of the local electron density n_e , becoming more negative when n_e increases. It is however also sensitive to electron temperature T_e , though the latter varies much less than n_e for the bulk cold population (Odelstad et al. 2015). Significant fluxes of energetic electrons may also add to the negative charging of the spacecraft. The negative values of the spacecraft potential over the selected period are anti-correlated

with the total neutral density n_C , which confirms previous findings (Odelstad et al. 2015). This also means that the electron density is correlated with the neutral density, which is consistent with equation (12). During period T1 on 2014 October 17, the potential is not as negative as anticipated, being given the intense neutral density peak. During period T2 on 2014 October 19, the potential is more negative than anticipated, being given the modest neutral density peak.

The count rates from the *RPC-IES positive ion spectrometer* are shown in the third panel from bottom in Figs 4 and 5 as a function of time and energy. The strong signal between 1 and 2 keV/ q corresponds to solar wind protons and the fainter one between 3 and 4 keV/ q is from solar wind alpha particles, He^{++} . These ions undergo significant deflections ($>45^\circ$) in the anti-sunward direction by interaction with the coma, with larger deflection for protons than for alpha particles (Broiles et al. 2015; Goldstein et al. 2015; Nilsson et al. 2015a,b; Behar et al. 2016). They may also be decelerated due to mass loading, though it does not seem significant here with detected energies corresponding to 400–600 km s $^{-1}$. A barely visible signal during period T1 on 2014 October 17 is seen just below 10 keV. It is also seen in the RPC-ICA data set for the same period (not shown). Additionally, a similar signal is observed between 00 and 12 UT on 2014 October 20 in fig. 2 of Broiles et al. (2015) with enhanced contrast. These high-energy peaks, which are detected when the neutral density is high, correspond to He^+ produced from the charge exchange of alpha particles with cometary neutrals (Shelley et al. 1987; Broiles et al. 2015; Burch et al. 2015; Goldstein et al. 2015; Nilsson et al. 2015a,b; Wedlund et al. 2016). At the lowest observed energy range between 4 and 20 eV, the large signal seen in RPC-IES ion spectra corresponds to water-group ions, as attested by the analysis of RPC-ICA (Nilsson et al. 2015a) and ROSINA-DFMS (Fuselier et al. 2015). The neutral velocity is typically 700 m s $^{-1}$ or less (see Section 3.3). This yields an energy of the order of 0.05 eV for newly born H_2O^+ ions, which is well below the RPC-IES lowest energy of 4 eV. Their detection is made possible thanks to the spacecraft potential, which accelerates them towards the detector. The maximum energy for the cometary ions as detected by RPC-IES is anti-correlated with ($-V_{\text{ph}}$): more negative spacecraft potential accelerates the cometary ions towards larger energies, as originally pointed out on RPC-ICA ion spectra (Nilsson et al. 2015a). With the not too negative spacecraft potential, the IES ion count rates undergo a modest acceleration during period T1. During period T2, with very negative spacecraft potential, there is evidence of large accelerations, though the peak in the ion count rate is located at a lower energy bin. While the cometary ion energy observed here is consistent with acceleration by the spacecraft potential [3/2 of ($-V_{\text{ph}}$), see Section 3.5], it does not exclude solar wind early pick-up process but limits its effect to the same order as the spacecraft potential. At larger cometocentric distances, the acceleration by the solar wind motional electric field has been detected with cometary ion energy reaching a few 100 eV or more (Goldstein et al. 2015; Nilsson et al. 2015a,b; Behar et al. 2016).

The count rates from the *RPC-IES electron spectrometer* are shown in the second panel from bottom in Figs 4 and 5 as a function of time and energy per charge. While the spectrometer operates above $E_{\text{min}} = 4$ eV, the negatively charged spacecraft potential rejects electrons with energies below $E_{\text{min}} + |V_{\text{sc}}|$. The data set presented here has not been corrected for the spacecraft potential, though for the quantitative analysis we have carried out, the electron flux density has been corrected (see Section 3.4.3). The hot electron population detected by RPC-IES includes various sources, such as photoelectrons – produced by solar EUV radiation in the coma – and solar wind electrons, all which may have been affected

by different acceleration mechanisms (Clark et al. 2015; Broiles et al. 2016b; Madanian et al. 2016). The RPC-IES electron count rates are found to be primarily anti-correlated with the ROSINA-COPS neutral density (including during period T1). After correction for the spacecraft potential, this anti-correlation is strongly attenuated but persists (see Figs 7 and 8). Nevertheless, during period T2, a correlation is found between the neutral density and the energetic electron count rates.

The *RPC-MAG* consists of two triaxial fluxgate magnetometers mounted on a 1.5 m boom (Glassmeier et al. 2007b). The lowest panel in Figs 4 and 5 shows the RPC-MAG magnetic field components of the outboard magnetometer in the CSEQ coordinates. Some spacecraft residual field is still present in the data set. As a result, spacecraft manoeuvres can be seen as, for instance, on 2014 October 19 between 07 and 11 UT, with sharp variations strongly correlated between the three components. Overall, the magnetic field does not show any extreme perturbations. On 2014 October 03–04, the magnetic field is quiet. On 2014 October 17, it exhibits large-scale variations and, during period T1, it undergoes a rotation about the z -axis. This short-scale structure corresponds to a large drop in the RPC-IES electron count rate. The count rate drop starts earlier but this earlier period is associated with a slew of the spacecraft which may not affect the largely isotropic electrons, but may have affected the magnetic field components. On 2014 October 18, it is more perturbed with higher RPC-IES electron count rates. There is some turbulence between 11 and 15 UT and a quieter time between 15 and 17 UT. The sharp transition seen in the magnetic field components around 18 UT is associated with a sharp drop in ($-V_{\text{ph}}$) and a sharp increase in the level of RPC-IES electron count rate (period T2). On 2014 October 20, after 16 UT, the large increase in the B_z component in CSEQ comes from a decrease in the B_y component in the spacecraft coordinates, pointing in the direction of the solar panels. It is visible on the inboard and outboard sensors in the same way. Thus, it seems to have an external source.

We have also checked the data set from the *Rosetta* Standard Radiation Environment Monitor (Mohammadzadeh et al. 2003). During the selected period, it is all quiet attesting of the absence of intense, energetic events, such as solar particle events.

3.3 Outflow velocity from MIRO

At the close cometocentric distances considered, we assume that the ions move radially outwards at the same velocity as the neutrals. The neutral outflow velocity u_n can be derived from *in situ* observations from ROSINA-COPS nude and ram gauges (Balsiger et al. 2007) and from remote-sensing observations from MIRO (Gulkis et al. 2007).

As the processing of the ROSINA-COPS neutral outflow velocities is still in progress, we are relying solely on the remote-sensing observations of the neutral outflow velocity from MIRO spectral observations. Based on the analysis of water rotational transition lines, it is possible to retrieve the mean water terminal expansion velocity. From the August 2014 data set with subsolar nadir pointing, Gulkis et al. (2015) and Lee et al. (2015) derived values for u_n between 600 and 800 m s $^{-1}$. Furthermore, Gulkis et al. (2015) found that the expansion velocity follows a diurnal behaviour similar to the one found for the neutral number density (see Section 3.2). Maximum values for u_n are observed when the neck is visible from the position of *Rosetta*. Moreover, Lee et al. (2015) found that the expansion velocity is positively correlated with outgassing intensity, while the terminal gas temperature is anti-correlated. These results are consistent with gas dynamics.

Biver et al. (2015) analysed the MIRO data set from 2014 September 7, at a heliocentric distance of 3.4 au, and associated with a phase angle of 90° , which corresponds to the geometry of our analysed data set. They found values for u_n from 470 to 590 m s^{-1} , lower than those derived for subsolar nadir pointing. The lowest values correspond to the nightside, while the largest values correspond to the neck and subsolar regions. To be conservative (with possible reduction in u_n in regions with increased CO_2) and owing to the smaller heliocentric distance in 2014 October (which would imply slightly larger u_n), we are considering values from 400 to 700 m s^{-1} for the outflow velocity and present the sensitivity of the modelled electron density for this range of values in Sections 4.2.1 and 4.2.2.

3.4 Ionization frequency

3.4.1 Neutral composition from ROSINA

At a heliocentric distance of 3 au and close to the comet (<20 km), we do not anticipate any significant neutral chemistry in the coma. This is confirmed by the analysis of ROSINA-DFMS, which does not show any evidence of dependence of the neutral composition – associated with volatile species – with r (Hässig et al. 2015). For instance, the CO/CO_2 number density ratio does not seem to increase with cometocentric distance. We have therefore assumed that the volume mixing ratios are independent of r .

The coma of comet 67P has been found to be strongly heterogeneous with variation in sub-spacecraft latitude and longitude of the main neutral species H_2O , CO and CO_2 , based on the analysis of ROSINA-DFMS (Hässig et al. 2015; Le Roy et al. 2015; Luspai-Kuti et al. 2015), ROSINA-Reflectron Time-of-Flight spectrometer (Mall et al. 2016) and VIRTIS (Bockelée-Morvan et al. 2015) at heliocentric distances of 2.5–3.5 au covering in particular the 2014 August–December period.

While overall water is the dominant species, there are times where CO_2 or CO is comparable to or even more abundant than water. CO number density variation mostly follows that of water, especially in the Northern hemisphere. CO_2 exhibits a different periodicity and dominates over water in regions of darkness of the Southern hemisphere (Hässig et al. 2015). Though solar insolation or the lack thereof may explain in part the larger dominance of super-volatiles, such as CO and CO_2 , sublimated from the cold regions of the winter, Southern hemisphere, it does not seem to be the only driver of the coma composition. Heterogeneity in the comet nucleus, either primordial or evolutionary as a result of differences in insolation over the orbital history, may also contribute to the dominance of CO_2 in the Southern hemisphere.

Though the composition varies in both latitude and longitude, the main difference is between the two hemispheres. The composition which we have applied is based on the two hemispheric cases reported by Le Roy et al. (2015): 2014 October 20 between 07:54 and 08:37 UT for the Northern hemisphere and 2014 October 19 between 00:39 and 01:22 UT for the Southern hemisphere, with volume mixing ratios given in Table 2. We have introduced a smooth transition between the two cases by the use of a linear interpolation between -10° and $+10^\circ$ latitude.

The composition of the coma is complex and rich, including numerous additional species, such as organics. However, their volume mixing ratios relative to water are less than a few per cent, often significantly less (Goesmann et al. 2015; Le Roy et al. 2015; Luspai-Kuti et al. 2015; Wright et al. 2015; Altwegg et al. 2016). O_2 , which was detected for the first time on a cometary coma by ROSINA-DFMS, is the fourth most abundant species at comet 67P

(Bieler et al. 2015a). The mean $\text{O}_2/\text{H}_2\text{O}$ value is 0.0380 ± 0.0085 and over the selected period it varies between 0.01 and 0.06. While some of the minor neutral species may be critical at higher outgassing rates for chemistry, such as NH_3 , CH_3OH or H_2S , with proton affinity higher than the affinity of water (Allen et al. 1987; Vignen & Galand 2013; Beth et al. 2016), they can be neglected in the estimation of the total ion production rates, only composition-dependent quantities in equation (12).

The effect of composition on the effective ionization frequencies, which depend on both the volume mixing ratios v_l and the COPS-composition parameter f_c , is discussed in Sections 3.4.2 and 3.4.3. The parameter f_c is applied to adjust the total number density derived from the ROSINA-COPS pressure nude gauge, for composition. It is defined as

$$f_c = \sum_l \frac{v_l}{\beta_l}, \quad (13)$$

where the factor β_l , given in Table 2, is the COPS response of the given neutral species l (H_2O , CO and CO_2) with respect to N_2 , the species used in the laboratory calibration of COPS.

3.4.2 Solar EUV photoionization frequency

EUV photons, up to wavelengths of 98 nm, have enough energy to ionize the main cometary neutrals, H_2O , CO_2 and CO (see Table 2). In a coma, dense enough to be optically thick at a given wavelength λ , the attenuated solar flux at that wavelength is calculated from the Beer–Lambert law. The optical depth at a wavelength $\lambda < 98$ nm over the EUV range at the solar terminator (phase angle = 90°) is less than 6×10^{-3} at the surface, for $\xi = 3 \times 10^{20} \text{ cm}^{-1}$, the highest observed activity parameter value during the selected period (see Table 1). This implies an attenuation of the solar spectral flux by less than 1 per cent. Even for $\xi = 3 \times 10^{21} \text{ cm}^{-1}$ to take into account the potentially larger values of n_n at lower phase angles on the path of the solar radiation, the attenuation is less than 6 per cent. For the period studied here, the atmosphere can therefore be considered optically thin to the solar EUV radiation and the photoionization frequency, to be independent of r .

The photoionization frequency for the neutral species l is derived from the observed solar spectral flux $F_{1\text{ au}}(\lambda)$ measured at Earth from Thermosphere Ionosphere Mesosphere Energetics and Dynamics (TIMED)/Solar EUV Experiment (SEE) (Woods et al. 2005):

$$\nu_{l,1\text{ au}}^{hv} = \int_{\lambda_{\min}}^{\lambda_l^{\text{th}}} \sigma_l^{hv,ioni}(\lambda) F_{1\text{ au}}(\lambda) d\lambda, \quad (14)$$

where $\sigma_l^{hv,ioni}(\lambda)$ is the total photoionization cross-section of the neutral species l associated with the threshold wavelength λ_l^{th} . The minimum wavelength value considered, λ_{\min} , is 0.1 nm. The cross-sections are from Vignen & Galand (2013) for H_2O and CO and from Cui et al. (2011) for CO_2 and refer to dissociative and non-dissociative ionization processes yielding singly charged ion species.

The effective photoionization frequency, $\nu_{1\text{ au}}^{hv}$, at 1 au is calculated from $\nu_{l,1\text{ au}}^{hv}$ by applying equation (7). Derived values for $\nu_{l,1\text{ au}}^{hv}$ for the three main neutral species considered are given in the last three columns of Table 1. Though the ionization frequency of CO_2 is almost double that of H_2O , taking into account the COPS-composition parameter, f_c , defined in equation (13), reduces this difference. For the period selected, 2014 October 03 corresponds to the low solar activity case, which yields lower effective photoionization frequencies than on 2014 October 19, which corresponds to the high solar activity case (see Table 1). The influence of composition on the

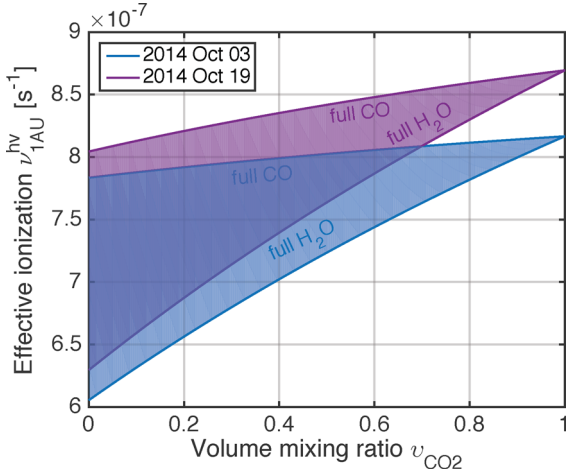


Figure 6. Effective photoionization frequency $\nu_{1\text{au}}^{hv}$ at 1 au for the lowest (2014 October 03 in blue) and highest (2014 October 19 in violet) solar activity cases during the selected period (see Table 1). The frequency is shown as a function of the volume mixing ratios of three neutral species, H_2O , CO and CO_2 . For a given day, the bottom (top) boundary of the given coloured area corresponds to $\nu_{1\text{au}}^{hv}$ (given on the y-axis), for a mixture of CO_2 (ν_{CO_2} given on the x-axis) and H_2O (CO) with a volume mixing ratio of $(1 - \nu_{\text{CO}_2})$. The values of $\nu_{1\text{au}}^{hv}$ in between these two extrema correspond to a mixture of the three neutral species, with a linear variation from H_2O to CO from the bottom to the top boundary (see also the text).

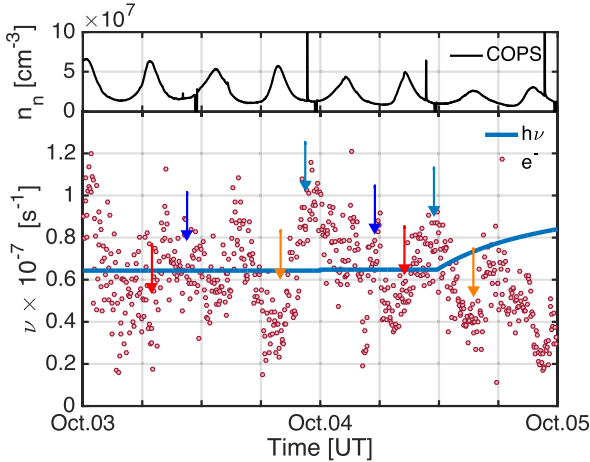


Figure 7. Top: ROSINA-COPS total neutral density $n_n(r_0)$ as a function of time. Bottom: effective electron-impact ionization frequency $\nu^e(r_0)$ (red circles) at the location of *Rosetta* and effective photoionization frequency ν^{hv} (blue solid line), as a function of time. The period shown is 2014 October 03–04. The vertical arrows point at the centre time of the period used to generate each averaged spectrum shown in Fig. 9. They have the same colour code as in Fig. 9.

effective ionization frequency at 1 au is illustrated in Fig. 6. The bottom boundary of the coloured area provides the effective photoionization frequency for a mixture of CO_2 (whose volume mixing ratio ν_{CO_2} is given on the x-axis) and H_2O ($\nu_{\text{H}_2\text{O}} = 1 - \nu_{\text{CO}_2}$), while the top boundary provides $\nu_{1\text{au}}^{hv}$ for a mixture of CO_2 (ν_{CO_2}) and CO ($\nu_{\text{CO}} = 1 - \nu_{\text{CO}_2}$). The values of $\nu_{1\text{au}}^{hv}$ vary linearly for a mixture of CO_2 , H_2O and CO between these two boundaries. For instance, on 2014 October 03, for a mixing ratio $\nu_{\text{CO}_2} = 0.2$, $\nu_{1\text{au}}^{hv}$ varies from $6.6 \times 10^{-7} \text{ s}^{-1}$ ($\nu_{\text{H}_2\text{O}} = 0.8$) to $7.9 \times 10^{-7} \text{ s}^{-1}$ ($\nu_{\text{CO}} = 0.8$). For a mixture of the three species, for instance $\nu_{\text{CO}_2} = 0.2$, $\nu_{\text{H}_2\text{O}} = 0.7$ and $\nu_{\text{CO}} = 0.1$, $\nu_{1\text{au}}^{hv} = (0.7 \times 6.6 \times 10^{-7} + 0.1 \times 7.9 \times 10^{-7}) / 0.8 =$

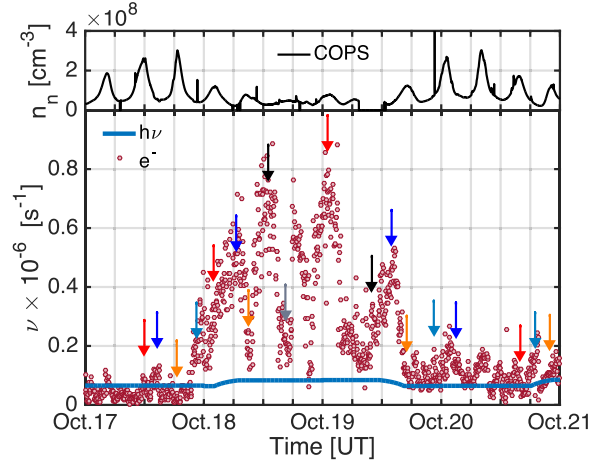


Figure 8. Same as Fig. 7 but for 2014 October 17–20.

$6.8 \times 10^{-7} \text{ s}^{-1}$. The frequency $\nu_{1\text{au}}^{hv}$ increases by a factor of 1.35–1.38 from pure H_2O (bottom boundary of a given coloured area with $\nu_{\text{CO}_2} = 0$) to pure CO_2 atmosphere ($\nu_{\text{CO}_2} = 1$), which illustrates the extreme summer to winter hemispheric cases for autumn 2014. It is also increased by the presence of CO from a pure H_2O atmosphere by a factor up to 1.30–1.33 ($\nu_{\text{CO}_2} = 0$).

The effective photoionization frequency, ν^{hv} , at comet 67P is derived from the frequency $\nu_{1\text{au}}^{hv}$ at 1 au by adjusting the solar flux in distance and in phase from the Earth to comet 67P. The heliocentric distance d_h has values around 3.2 au. We also apply a shift in days, δ_{Earth} , due to the phase angle ϕ_{Sun} between the Earth, the Sun and comet 67P ranges from 5 to 6 d (see Table 1). For instance, for 2014 October 03 at comet 67P, we use the TIMED/SEE solar flux measured at Earth on 2014 October 08. The frequency ν^{hv} is compared to the electron-impact ionization frequency at the location of the *Rosetta* spacecraft in Section 3.4.3.

3.4.3 RPC-IES electron-impact ionization frequency

The electron-impact ionization frequency at the location of *Rosetta* is derived from the hot electron intensity I_e^{IES} measured by RPC-IES electron spectrometer (Burch et al. 2007; Broiles et al. 2016a; Madanian et al. 2016). For a given neutral species, it is calculated as follows:

$$\nu_l^e(r_0) = \int_{E_l^{\text{th}}}^{E_{\text{max}}} \sigma_l^{e,\text{ioni}}(E) J_e(r_0, E) dE, \quad (15)$$

where $J_e(r_0, E)$ is the electron flux density at the cometocentric distance r_0 of *Rosetta*. $J_e(r_0, E)$ is derived from I_e^{IES} after integration over elevation and azimuthal angles and assuming isotropy for blind spots due to obstruction or out of the field of view (Clark et al. 2015). It is also corrected for the spacecraft potential by applying equation (16) discussed just below. The electron-impact ionization cross-sections $\sigma_l^{e,\text{ioni}}(E)$ are from Vigren & Galand (2013) for H_2O and CO and from Cui et al. (2011) for CO_2 and refer to dissociative and non-dissociative ionization processes yielding singly charged ion species. The bottom boundary energy, E_l^{th} , is the ionization threshold associated with the single, non-dissociative ionization of the neutral species l yielding the ion species in the ground state (see Table 2). The top boundary energy, E_{max} , is set to 200 eV. Beyond this energy, the count rate is very low and $J_e(r_0, E)$ reaches the noise level. It also corresponds to an energy range over which electron-impact cross-sections decrease with energy. We have checked that

the ionization frequency values are not significantly changed if E_{\max} extends up to 17 keV, the maximum energy of RPC-IES electron spectrometer.

As attested by RPC-LAP (see Section 3.5), the spacecraft is charged negatively during the selected period (see Figs 4 and 5) repelling electrons from the ‘natural’ plasma and affecting its distribution. The RPC-IES electron spectra are affected by the presence of this negatively charged spacecraft potential. Applying Liouville’s theorem to the close environment of the spacecraft, the phase space density $f_e(\mathbf{r}, \mathbf{v})$ is conserved along the electron’s trajectory (Génot & Schwartz 2004), that is, its Lagrangian derivative: $\frac{df_e}{dt} = 0$. The cometocentric distance r_0 of *Rosetta* of 10–20 km is significantly larger than the extent of the charged cloud around the spacecraft of a few metres (see Section 3.5). Therefore, assuming that the electron trajectories are not appreciably deflected, Liouville’s theorem implies that the quantity $J_e(\mathbf{r}, E)/E$ is conserved from some position outside the spacecraft plasma sheath to the position \mathbf{r}_{IES} of the detector. Note that the electron number flux density is given by $J_e(\mathbf{r}, E) = \left(\frac{v^2}{m}\right) f_e(\mathbf{r}, v)$. Under the assumption that the trajectories are radial with respect to the spacecraft, this implies

$$J_e(r_0, E) = \frac{E}{E_{\text{IES}}} J_e^{\text{IES}}(r_{\text{IES}}, E_{\text{IES}}). \quad (16)$$

Equation (16) enables us to reconstruct the free-space electron number flux near the spacecraft from the measured fluxes. E_{IES} is the energy of the electrons as measured by IES and $E = E_{\text{IES}} - V_{\text{SC}}$ is the ‘free-space’ energy. V_{SC} , negative quantity here, is the true spacecraft potential with respect to infinity (see Section 3.5), as RPC-IES is located directly on the spacecraft. The values for V_{SC} are derived from the analysis of RPC-LAP measurements, as explained in Section 3.5. As the spacecraft potential is negative, the correction implies a shift of the RPC-IES electron spectra towards higher energies. When the energy shift induced by the V_{SC} correction yields a minimum energy E_{\min}^c above the ionization threshold energy E_l^{th} (see Table 2), a constant value for $J_e(r_0, E)$ equal to the one at the lowest energy bin is assumed between E_l^{th} and E_{\min}^c in order to apply equation (15). This affects times when the spacecraft potential is very negative, that is, typically when the neutral number density is large or during period T2 (see Figs 4 and 5). The extrapolation towards lower energies, down to the ionization threshold, increases the electron-impact ionization frequency up to a factor of 2. The values of the electron-impact ionization frequency are also affected by the analysis of the Microchannel Plate Detector efficiency – which varies with energy and increases v_e^i by up to 50 per cent –, the choice of azimuthal and elevation bins – as some directions suffer from blockage – (Broiles et al. 2016a), and the assumptions made for the electron flux density over the missing field of view. Follow-up studies are planned to try to further constrain these sources of uncertainty.

The effective electron-impact ionization frequency $v_e^e(r_0)$ at the location of *Rosetta* is calculated from the species-dependent frequencies $v_f^e(r_0)$ by applying equation (8). The derived values are plotted with red circles in the bottom panel of Fig. 7 for 2014 October 03–04 and of Fig. 8 for 2014 October 17–20. Data points are spaced by 4 min and 16 s, which corresponds to the RPC-IES electron sampling time. For comparison, the effective photoionization frequency v^{hv} – defined in Section 3.4.2 – is shown with blue lines. Its variation from one day to another results from changes in the daily solar flux, and its variation over the course of a day is associated with variation in neutral composition (see Section 3.4.1).

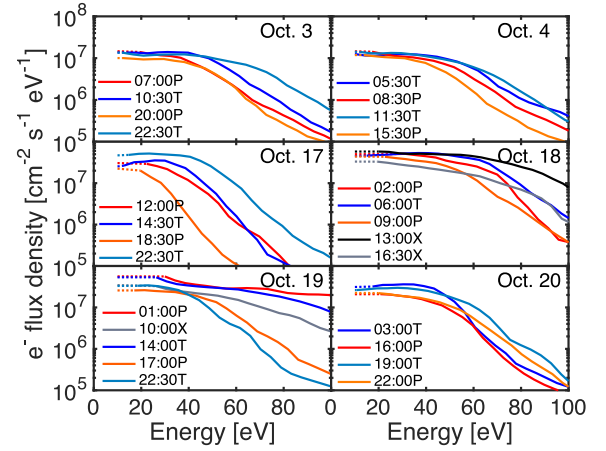


Figure 9. Mean RPC-IES electron spectra $\langle J_e(r_0, E) \rangle$ for each selected day. They are the result of a moving average filter over nine RPC-IES spectra, after they were corrected for the spacecraft potential V_{SC} . The time indicated corresponds to the centre time of the averaging period. Each individual spectrum is extrapolated – when needed – from the lowest energy bin – which is a function of the S/C potential – down to 10 eV. The mean spectra are plotted with dotted lines below the lowest energy bin of the centre time spectrum. ‘P’ (orange and red spectra) and ‘T’ (blue spectra) refer to ‘Peak’ and ‘Trough’ seen at the same time in the ROSINA-COPS neutral number density, $n_n(r_0)$ (see Figs 7 and 8). The spectra identified by ‘X’ and shown in black and grey correspond to periods in the Southern hemisphere where no semi-diurnal variations were identified. The spectrum at 18:30 UT on 2014 October 17 is within the period T1 and the spectrum at 01:00 UT on 2014 October 19 is within the period T2.

Over the northern, summer hemisphere, the local electron-impact ionization frequency $v_e^i(r_0)$ is generally anti-correlated with the ROSINA-COPS total neutral density $n_n(r_0)$. On 2014 October 03–04, at a cometocentric distance of about 20 km, the anti-correlation is very strong, while it is significantly weaker on 2014 October 17 (including period T1), and disappears over part of 2014 October 20 at a cometocentric distance of about 10 km. In addition, the local electron-impact ionization frequency $v_e^i(r_0)$ is of the same order as the effective photoionization frequency with the bulk of the values within a factor ranging from 0.5 to 2 of v^{hv} .

Over the mid-latitude, southern, winter hemisphere (period T2, see Fig. 5), when the neutral density $n_n(r_0)$ is the weakest, the local electron-impact ionization frequency $v_e^i(r_0)$ is correlated with $n_n(r_0)$. Furthermore, over the full Southern hemisphere (from 06 UT on 2014 October 18 to 12 UT on 2014 October 19), the local electron-impact ionization frequency $v_e^i(r_0)$ reaches values at its peaks which are a factor of 5–10 times the effective photoionization frequency v^{hv} .

To get further insights on the origin of the local electron-impact frequency magnitude and variation, ‘typical’ spectra are shown at ROSINA-COPS $n_n(r_0)$ peaks (P) or troughs (T) or at other interesting times (‘X’) in Fig. 9. Each spectrum results from the average of nine RPC-IES electron flux densities. The times given in UT correspond to the central time of the averaging period, that is, the time of the fifth spectrum. They are also shown as vertical arrows in Figs 7 and 8 with the same colour code. The spectra have been corrected for the spacecraft potential with extrapolation towards lower energies shown as dotted lines in Fig. 9.

Over the northern, summer hemisphere, the electron flux densities associated with n_n peaks have usually lower values than those associated with n_n troughs, confirming the anti-correlation observed

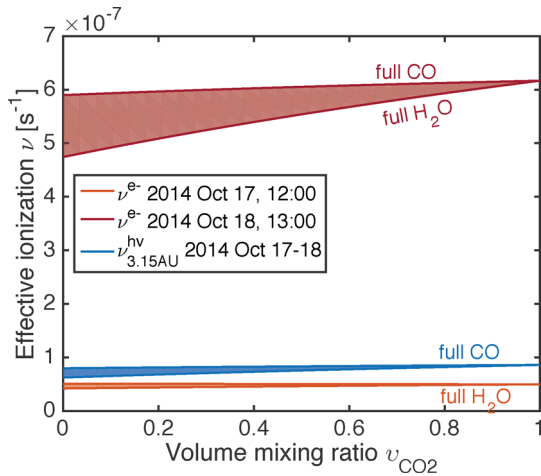


Figure 10. Effective electron-impact ionization frequency ν^e for a low RPC-IES electron level (12 UT on 2014 October 17, in orange) and a high one (13 UT on 2014 October 18, in red). The effective photoionization frequency ν^{hv} for 2014 October 17–18, at a heliocentric distance of 3.15 au, is shown in blue. The ionization frequencies are shown as a function of the volume mixing ratio ν_{CO_2} combined with a mixture of H_2O (bottom boundary) and of CO (top boundary).

between $\nu^e(r_0)$ and $n_n(r_0)$. On 2014 October 20, above 55 eV, the P and T spectra cross over and the correlation around $\nu^e(r_0)$ and $n_n(r_0)$ disappears. On 2014 October 03–04, the spectra associated with the troughs are shallower compared with those on 2014 October 17 and 2014 October 20 and reach higher electron flux densities. The spectra associated with the peaks are however more similar between 2014 October 03–04, 2014 October 17 (12:00 UT) and 2014 October 20. Finally, during period $T1$ (18:30 UT on 2014 October 17), the electron spectrum is very steep with very low electron flux density beyond 50 eV. It seems therefore that the trough spectra on 2014 October 03–04 are associated with hot electrons which have suffered the least energy degradation, while during period $T1$ associated with the highest total number density $n_n(r_0)$ (and highest ξ , see Fig. 5), the hot electrons have undergone the most energy degradation.

Over the southern, winter hemisphere, the electron flux densities have values higher than those observed at the same cometocentric distance on 2014 October 17 and 2014 October. In particular, extremely large values are observed at 13:00 UT on 2014 October 18 and over the whole morning of 2014 October 19, while the neutral density $n_n(r_0)$ is low. During period $T2$ on 2014 October 19, associated with a peak, though weak, the electron density flux is the highest, consistent with the correlation between $\nu^e(r_0)$ and $n_n(r_0)$ observed during this period. The high flux densities may be due to heating by lower hybrid waves (Broiles et al. 2016b).

The effect of composition on the electron-impact ionization frequency is illustrated in Fig. 10 where two electron-impact cases are shown: one during a period of low electron flux density (12:00 UT on 2014 October 17, in orange) and the other during a period of high electron flux density (13:00 UT on 2014 October 18, in red). Average spectra associated with these two periods are shown in Fig. 9. For reference, the photoionization frequency representative of 2014 October 17–18, at a heliocentric distance of 3.15 au, has been added in blue. Similarly to what was found for photoionization (see Section 3.4.2), the electron-impact ionization frequency ν^e of CO_2 is slightly higher than that of CO, and the smallest values are found for H_2O .

3.5 RPC-LAP electron density

The RPC-LAP instrument consists of two Langmuir probes mounted on two booms of approximately 2 m length (Eriksson et al. 2007). Besides the electrons from the natural plasma environment, photoelectrons are emitted by the spacecraft and from the probes. A charge sheath is formed around the spacecraft. Being negative during the period selected, it repels electrons. In the tenuous neutral density environment encountered at 3 au, for an electron temperature of 7 eV and an electron density of 400 cm^{-3} , the Debye length is about 1 m. The charge sheath extends typically to a radius of three times the Debye length, that is, to about 3 m for the plasma conditions encountered by *Rosetta* during the period under study (Odelstad et al. 2016). The spacecraft potential field decays therefore beyond the location of the sensors. The potential ($-V_{\text{ph}}$) from the spacecraft to the Langmuir probe is assumed to be $2/3$ of the true spacecraft potential V_{SC} with respect to infinity, based on the Debye length compared to the boom length, by assuming a constant spacecraft photoemission current density of 8.3 nA cm^{-2} – corresponding to the average of the photoemission current density from the Langmuir probes during the time interval under consideration in this study – and finding the ambient electron density n_e required to produce a current of impacting plasma electrons on the spacecraft body which exactly balances this photoemission current density at the observed spacecraft potential V_{SC} .

The electron number densities are derived from the observed V_{ph} , also referred to as the photoelectron knee potential (Eriksson et al. 2007; Odelstad et al. 2015). The potential ($-V_{\text{ph}}$) is shown in the fourth panel from top in Figs 4 and 5. A factor $3/2$ is applied to ($-V_{\text{ph}}$) to provide the full V_{SC} , from which density values representative of the actual electron density in the ambient plasma, unperturbed by the presence of the spacecraft, can be derived. Using the spacecraft potential to derive the electron density in this way requires the assumption of a value for the electron temperature, T_e . In addition, any contribution by energetic electrons to V_{SC} is neglected, resulting in possible overestimation of n_e at a given assumed T_e during periods of high electron flux densities in the RPC-IES spectra. Though the bias voltage sweeps offer the possibility to derive T_e independently (Eriksson et al. 2007), the uncertainties on the derived T_e for the selected period are too large to be used. The choice of T_e to derive n_e is discussed in Section 4.1.

3.6 RPC-MIP electron density

The RPC-MIP instrument and its working principle are described in detail in Trotignon et al. (2007) and references therein. In October 2014, RPC-MIP was operating in the Long Debye Length (LDL) mode every other day for a duration of 10 or 12 consecutive hours. In this mode, RPC-MIP uses RPC-LAP2 as electric transmitter and receives the signal on the RPC-MIP antennas located about 4 m away. This mode is designed to probe a plasma with a Debye length of less than about 2 m, which is suitable for the period of 2014 October for which the Debye length is of the order of 1 m (see Section 3.5).

The plasma density retrieved when using the LDL mode of the RPC-MIP experiment is however limited at both high and low number densities. First, the mutual impedance spectra are flat with respect to frequency – as expected in vacuum – when the Debye length gets close to the distance between the electric emitters and the receivers. In this case, the MIP experiment becomes blind to the plasma. This happens for a small enough number density: in the case of 7 eV electrons and in LDL mode, this lower threshold

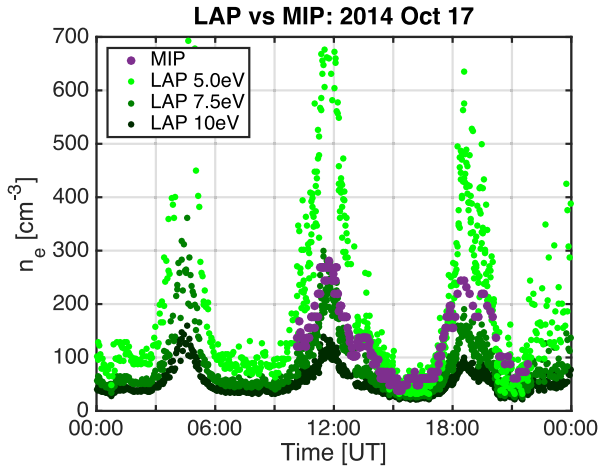


Figure 11. Comparison of the electron density from RPC-MIP (large violet points) and RPC-LAP (small green points) for 2014 October 17. The RPC-LAP electron density values are derived assuming an electron temperature T_e of 5 eV (light green), 7.5 eV (medium green) and 10 eV (dark green).

is around 50 cm^{-3} . Secondly, the frequency range is limited to the interval [7–168] kHz in the LDL operational mode, so that plasma densities higher than about 350 cm^{-3} cannot be detected.

The electron number densities are derived from the estimated position of the plasma frequency in the MIP complex (amplitude and phase) mutual impedance spectra, obtained at a cadence of about 10 or 3 s depending on the day (normal and burst modes, respectively). To filter out the short time-scale compressible plasma dynamics and highlight the low-frequency density variations associated with the ionization of the cometary expanding atmosphere, moving median values of the electron density have been computed from consecutive density measurements. These are the values presented in Section 4. No adjustment has been made on the RPC-MIP electron density measurements regarding the possible effect of the depleted electron sheath around the (negatively charged) spacecraft, which is still under investigation.

4 COMPARISON BETWEEN RPC-LAP, RPC-MIP AND MODELLED ELECTRON DENSITIES

4.1 Comparison between RPC-LAP and RPC-MIP

Fig. 11 shows the electron density n_e measured by RPC-MIP (violet dots) and by RPC-LAP for three different assumed electron temperatures T_e , 5 eV (light green), 7.5 eV (medium green) and 10 eV (dark green), on 2014 October 17. An electron temperature of 10 eV is a good approximation for the temperature of photoelectrons produced in the coma and which have not undergone energy degradation. We checked this by calculating the second moment of the energetic electron distribution using the electron transport model of Vigren & Galand (2013) in an optically thin atmosphere in the EUV and for the solar flux from 2014 October 17. Here we disregard photoelectrons produced from photoemission and which have typical energies of 2–3 eV upon release from the surface (Feuerbacher et al. 1972). At the heliocentric distance considered, the bulk of the photoelectrons can be attributed to the coma.

On 2014 October 17, between 10 and 22 UT both RPC-LAP and RPC-MIP (mode LDL) were operating. This is the only overlapping period between these two sensors when *Rosetta* was close to comet

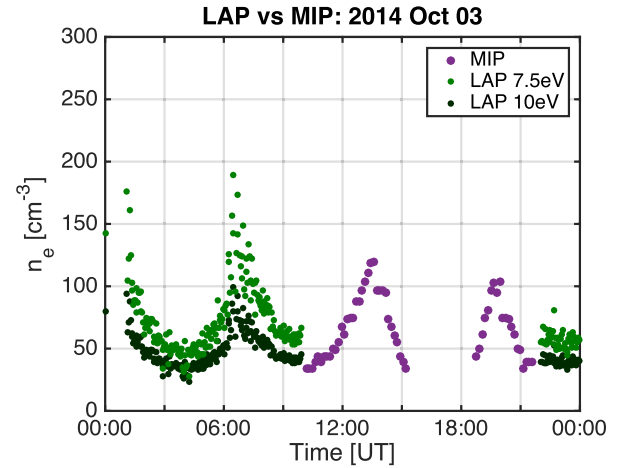


Figure 12. Same as Fig. 11 but for 2014 October 03. The RPC-LAP electron density is shown for two T_e values: 7.5 eV (medium green) and 10 eV (dark green).

67P in 2014 October. The RPC-LAP n_e fits well the RPC-MIP for $T_e = 7.5 \text{ eV}$ for the periods around the peak near 12 UT and the trough near 15 UT. The typical spectra around these periods are also similar, as attested by Fig. 9. However, around the peak near 18:30 UT – corresponding to period T1 (see Fig. 5), an electron temperature lower than 7.5 eV, though higher than 5 eV, is required to have RPC-LAP electron density matching the density from RPC-MIP. This result is consistent with the steeper electron spectrum seen at 18:30 UT in Fig. 9 and a larger energy degradation of the electron population. Near the 21:30 UT trough, the RPC-LAP electron density values from different assumed T_e overlap partially. However, the best match between RPC-LAP and RPC-MIP is reached for an electron temperature of 7.5 eV.

Fig. 12 shows the electron density n_e from RPC-MIP (violet dots) and RPC-LAP (green dots) on 2014 October 03. Their values are half those on 2014 October 17. While the activity parameter ξ is of the same order of magnitude on both days (see Table 1), the cometocentric distance of *Rosetta* is double the distance on 2014 October 17. This is consistent with the $1/r$ dependence obtained in equation (12). The absence of RPC-MIP data between 15:00 UT and 18:30 UT is the result of the electron density being below the sensitivity of the RPC-MIP in the LDL mode (see Section 3.6). The troughs near 10:30 UT and near 22:00 UT correspond to the transition between the RPC-LAP and RPC-MIP (mode LDL) operation. During these two periods, an electron temperature of 10 eV yields RPC-LAP electron density (dark green dots) to match well the RPC-MIP electron density. This is consistent with the high electron flux density – with moderate energy slope – observed during these periods (see Fig. 9). Nevertheless, during peak periods on 2014 October 03, the electron spectra seem more similar to those observed at 12:00 and 14:30 UT on 2014 October 17. The latter are associated with $T_e = 7.5 \text{ eV}$ (see Fig. 11). Therefore, the peak periods on 2014 October 03 are more likely to be associated with a similar T_e .

Fig. 13 shows the electron density n_e from RPC-MIP (violet dots) and RPC-LAP (green dots) on 2014 October 19. Saturated electron density values present between 00 and 03 UT – belonging to period T2 – and reaching 837 cm^{-3} ($T_e = 7.5 \text{ eV}$) have been removed. They result from a saturation effect associated with very negative values of the spacecraft potential outside the measurement range of RPC-LAP (see Fig. 5). The remaining values around

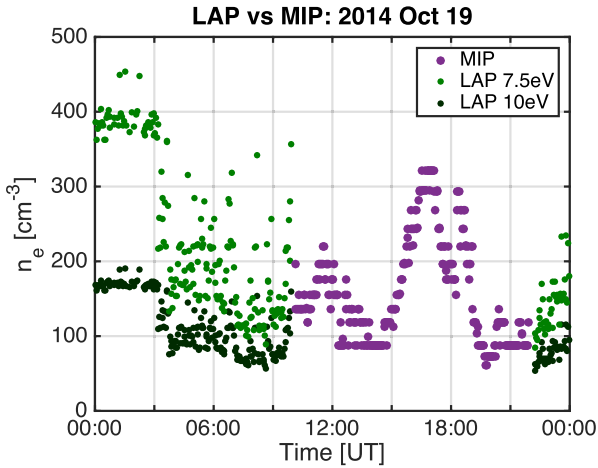


Figure 13. Same as Fig. 11, but for 2014 October 19. The RPC-LAP electron density is shown for two T_e values: 7.5 eV (medium green) and 10 eV (dark green).

350–450 cm^{-3} ($T_e = 7.5$ eV) are not saturated, though they are close to the saturation limit and might be possibly underestimated. The erroneous values are associated with electron density values higher than the undersaturated values shown on the plot. Between 03:00 UT and 09:30 UT on 2014 October 19, the electron density is very perturbed. This period during which RPC-LAP was operating is followed by a less disturbed period when RPC-MIP was operating in LDL mode. Furthermore, *Rosetta* underwent large manoeuvres between 07:25 and 12:15 UT. It seems difficult to infer the most suitable electron temperature for the RPC-LAP data set on 2014 October 19, in the morning. It is unlikely though that T_e would be lower than 7.5 eV: (1) this would yield an electron density too high to be consistent with the RPC-MIP at 10 UT; (2) the RPC-IES energetic electron flux densities are very intense (see Fig. 9); (3) though

ROSINA-COPS was not operating during the RPC-LAP to RPC-MIP transition, the neutral number density is modest compared with the summer hemisphere days during which an electron temperature of 7.5 eV was found to be suitable (putting aside the period T1). This is also supported by RPC-MIP, which was operating in Short Debye Length mode (not shown). This mode is targeting colder and higher density electrons not observed in 2014 October, therefore providing a very noisy data set during this period, at the limit of the instrument sensibility. However, before 04 UT on 2014 October 19, it is possible to infer that the plasma frequency is between 150 and 200 kHz, meaning that the electron density is of the order of 300–500 cm^{-3} before 03–04 UT, which is consistent with the RPC-LAP data set assuming $T_e = 7.5$ eV. At the end of the RPC-MIP period, at 22 UT, an electron temperature of 7.5 eV for RPC-LAP also ensures the plasma density continuity from RPC-MIP to RPC-LAP density measurements.

4.2 Model–observation comparison of the electron density

The ROSINA-COPS total neutral number density n_n (solid line) and the sub-spacecraft latitudes (dashed line) are plotted in the top panel of Figs 14–16, for 2014 October 03–04, 2014 October 17–18 and 2014 October 19–20, respectively. The comparison between the electron density observed by RPC-MIP (violet dots), RPC-LAP (green dots) and calculated (coloured areas) is shown in the bottom panel of Figs 14–16. The electron density, derived from equation (12) as illustrated in Fig. 2, is shown in blue when the model is driven by solar EUV photoionization alone ($\nu^e = 0$) and in red when the model is driven by both photo- and electron-impact ionization. The latter is derived from RPC-IES at $r = r_0$ and the ionization frequency ν^e is assumed to be independent of r . The implication of such an assumption is discussed in Section 5. The spread in modelled values for a given case (pure solar photoionization or photo- and electron-impact ionization) results from the range of values

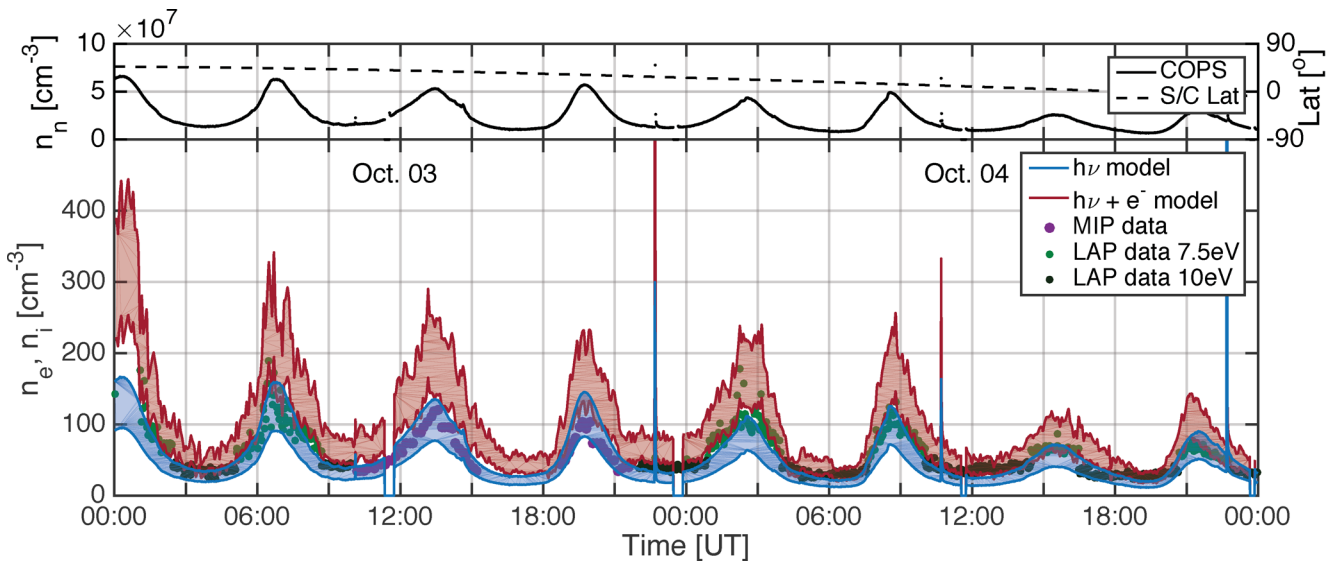


Figure 14. Top: ROSINA-COPS total neutral number density $n_n(r_0)$ and the sub-spacecraft latitude as a function of time. Bottom: ionospheric density as a function of time. The period shown is 2014 October 03–04. The blue (red) curves correspond to the calculated ionospheric density assuming photoionization alone (photoionization and electron-impact ionization). The vertical spread of these curves corresponds to the range of ion outflow velocity considered, spreading from 400 m s^{-1} (top boundary) to 700 m s^{-1} (bottom boundary). The RPC-MIP electron density is shown with large, violet dots. There are no RPC-MIP data between 15:00 and 18:30 UT as the electron density was too low to be detected by the sensor in the LDL mode. The RPC-LAP electron density is shown with small green dots, assuming an electron temperature of 7.5 eV (light green for $\xi \geq 7 \times 10^{19} \text{ cm}^{-1}$) or 10 eV (dark green for $\xi < 7 \times 10^{19} \text{ cm}^{-1}$) (see Section 4.1).

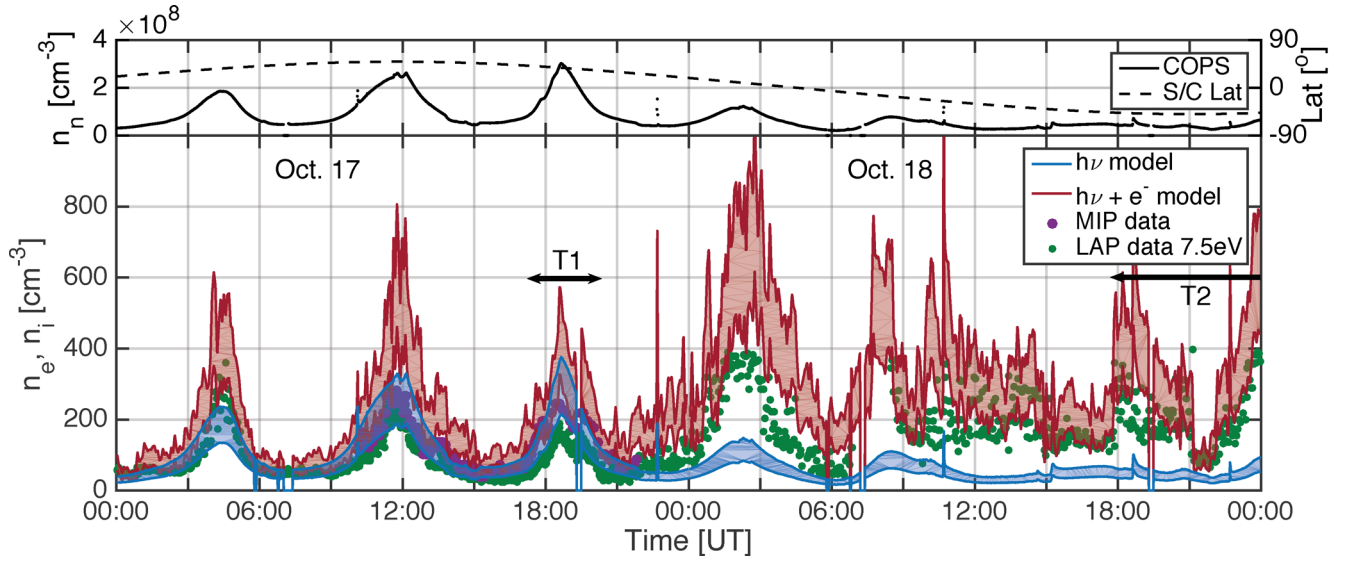


Figure 15. Same as Fig. 14 but for 2014 October 17–18. The RPC-LAP electron density is associated with an electron temperature of 7.5 eV. Due to a different operation mode, there is no RPC-LAP electron density available between 07:00 and 08:30 UT on 2014 October 18. The periods of interest, T1 and T2 – which ends on 2014 October 19 – are identified by horizontal arrows.

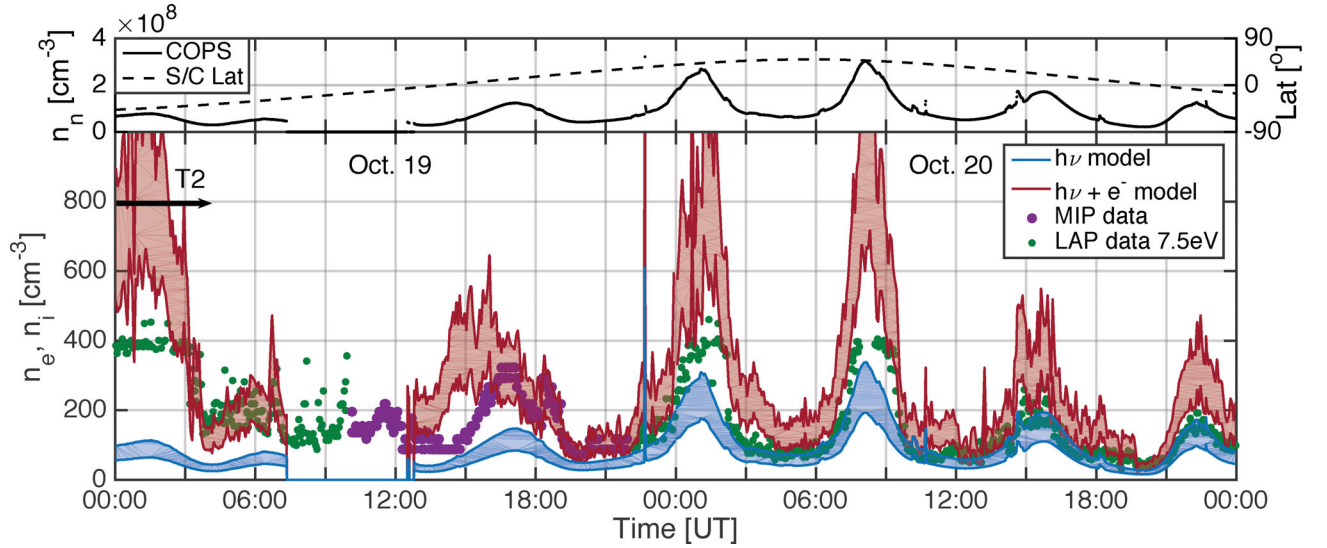


Figure 16. Same as Fig. 14 but for 2014 October 19–20. The RPC-LAP electron density is associated with an electron temperature of 7.5 eV. Due to large manoeuvres, ROSINA-COPS was not operating between 07:25 and 12:15 UT on 2014 October 19. The period of interest T2 – which starts on 2014 October 18 – is identified by a horizontal arrow.

considered for the ion–neutral outflow velocity, from 400 m s^{-1} (top boundary) to 700 m s^{-1} (bottom boundary), based on MIRO data analysis from 2014 September (see Section 3.3).

In Fig. 14 (2014 October 03–04), the RPC-LAP electron density is derived from an electron temperature T_e of 10 eV for $\xi < 7 \times 10^{19} \text{ cm}^{-1}$ and of 7.5 eV for larger ξ , as justified in Section 4.1. In Figs 15 and 16 (2014 October 17–20), the RPC-LAP electron density is derived assuming a constant T_e of 7.5 eV for simplification, though such a value is too high around period T1 (near 18:30 UT on 2014 October 17, see Fig. 4) and is uncertain during period T2 (from 18 UT on 2014 October 18 to 04 UT on 2014 October 19, see Fig. 5), as discussed in Section 4.1. Finally, between 07 and 10 UT on 2014 October 20, flat electron density values have been removed due to saturation, similarly to the 00–03 UT period on 2014 October 19, as discussed in Section 4.1.

4.2.1 Northern, summer hemisphere

Over the northern, summer hemisphere (2014 October 03–04, 2014 October 17 and 2014 October 20), the electron density n_e measured by RPC-LAP (green dots) and RPC-MIP (violet dots) is strongly correlated with the total neutral density n_n (black line) (see Figs 14 and 15), confirming earlier findings (Edberg et al. 2015; Vigren et al. 2016). The observed electron density follows the semi-diurnal variation exhibited by the total number density, as discussed in Section 3.2. In addition, secondary, sharp peaks are seen in both the observed neutral density and electron density, such as at 10 UT on 2014 October 17 (see also Fig. 11 where the observed electron density peak is more visible), while others are only seen in the observed electron density, such as around 13:30 UT on 2014 October 17 (see Fig. 11). While the former may be associated with local

ionization resulting from spacecraft outgassing during manoeuvres, the latter may result from the contribution of energetic electrons whose level is increased over this period, though their increase starts already from 12 UT.

Regarding model–observation comparison, on 2014 October 03–04 and on 2014 October 17, the ionospheric density driven by photoionization alone (blue curves) agrees very well with the RPC-MIP electron density within the uncertainty in ion outflow velocity. The electron density driven by both photoionization and electron-impact ionization (red curves) overestimates the observed electron density. Solar EUV radiation is therefore the main source of ionization, and the contribution by electron-impact ionization – assumed constant with r in the model – is largely overestimated; the independence of ν^e with r is discussed in Section 5. Furthermore, the very good agreement between the photoionization model and RPC-LAP at the peak densities (excluding period T1) attests that an electron temperature of 7.5 eV seems to be a good assumption over these three days. For period T1 around the peak near 18:30 UT on 2014 October 17, only RPC-MIP electron density should be considered. Indeed, by comparing RPC-MIP and RPC-LAP (see Section 4.1), we inferred that T_e is lower than the value of 7.5 eV assumed to drive the RPC-LAP electron density in Fig. 15. Finally, note that the electron density peak near 18:30 UT has lower values than the one at 12:00 UT, though the former is associated with a higher neutral density. As pointed out in Section 3.3, higher activity parameter ξ corresponds to higher outflow velocity. Based on equation (12), for a given cometocentric distance r , the ionospheric density is proportional to n_n , that is, to ξ , and inversely proportional to the outflow velocity. The activity parameter ξ increases by 15 per cent from 2.6×10^{20} to $3.0 \times 10^{20} \text{ cm}^{-1}$ from the 12:00 UT to the 18:30 UT peak. Therefore, an increase in outflow velocity by more than this percentage, for instance from 550 to 650 m s^{-1} (18 per cent increase), would overcome the ξ increase and would decrease n_i . This result is consistent with the fact that the ionospheric density near 18:30 UT is close to the bottom boundary of the solar EUV-driven modelled electron density.

On 2014 October 20, the modelled electron density driven by photoionization alone agrees reasonably well with the observed electron density after noon, but underestimates them significantly at earlier times, especially between 01 and 02 UT and 08 and 10 UT. This is all the more true for the peak around 08 UT where saturated electron density values have been removed but are anticipated to be higher than the unsaturated ones shown. Higher T_e would decrease RPC-LAP n_e . However, because the peak neutral density has values similar to those reached on 2014 October 17, it is unlikely that T_e would be higher than 7.5 eV in the morning of 2014 October 20. During this period, the effective electron-impact ionization frequency ν^e has higher values than observed on 2014 October 17 (see Fig. 8). This may indicate that electron-impact ionization contributes to the ionospheric density in the morning of 2014 October 20. What is puzzling though is that at the electron density peak near 22:30 UT and associated with a modest neutral density, the agreement between the observed and photoionization modelled electron density is good, while the frequency ν^e remains of the same order over the course of the day (see Fig. 8).

4.2.2 Southern, winter hemisphere

2014 October 18 and 19 are primarily over the southern, winter hemisphere, with an excursion towards the Northern hemisphere in the early morning of 2014 October 18 and in the afternoon and

evening of 2014 October 19 (see the top panel of Figs 15 and 16). We discuss 2014 October 19 first as during that day there are RPC-MIP electron density measurements which are independent of T_e .

On 2014 October 19 (see Fig. 16), the ionospheric model driven by solar photoionization alone (blue curves) cannot explain the electron density observed by RPC-MIP (violet dots), even when low outflow velocity values expected in the winter hemisphere are considered (corresponding to the top boundary of the blue area). The RPC-MIP peak electron density reaches values above 300 cm^{-3} associated with a neutral number density of $1.2 \times 10^8 \text{ cm}^{-3}$, while on 2014 October 17, the largest electron density peak at 12:00 UT reaches values just below 300 cm^{-3} and is associated with a neutral density of $2.6 \times 10^8 \text{ cm}^{-3}$, more than double the density near the 2014 October 19 peak. The variation in u_i cannot however explain alone the difference as pointed out above. While the ionospheric model driven by both solar photoionization and electron-impact ionization (red curves) overestimates the RPC-MIP electron density (green dots) between 13:00 and 16:30 UT, it agrees with it afterwards, though a high outflow velocity is required (bottom boundary of the red area). As the activity parameter is modest, it is unlikely that the velocity is very high (see Section 3.3). This may indicate that the contribution from energetic electrons is slightly overestimated by the ionospheric model, though significant. Furthermore, the RPC-MIP electron density (violet dots) exhibits a local peak just after 18 UT which is not present in the neutral density (black line) but is captured by the ionospheric model which includes electron-impact ionization (red curves). This is also the case for the peak near 15 UT, though the peak only appears on the RPC-MIP electron density before high-frequency filtering (not shown) and is no longer present in the final product presented in Fig. 16. All this attests to the significant contribution from energetic electrons as a source of ionization between 12 and 22 UT on 2014 October 19 (see Fig. 8).

Between 03 and 07 UT on 2014 October 19, the ionospheric model driven by both solar photo- and electron-impact ionization (red curves) agrees well with the RPC-LAP observations (green dots) with the temperature T_e taken to be 7.5 eV, as justified in Section 4.1. This is consistent with what was found in the afternoon with the RPC-MIP data set (violet dots). Between 00 UT and 03 UT – covering part of period T2 –, the ionospheric model driven by both ionization sources overestimates the RPC-LAP density. Over this period, saturation is occurring and the removed saturated RPC-LAP data set is associated with electron density values higher than those shown on the plot from the unsaturated data set, as discussed in Section 4.1. The large contribution from electron impact in the morning of 2014 October 19 is consistent with the large RPC-IES electron flux densities observed during this period (see Fig. 9) and resulting in very large effective electron-impact ionization frequencies at the location of *Rosetta*, up to a factor of 10 higher than the effective photoionization frequency (see Fig. 8).

After 08:30 UT on 2014 October 18 (see Fig. 15), the ionospheric model including electron-impact ionization agrees well with the RPC-LAP electron density ($T_e = 7.5 \text{ eV}$), similar to what was found on 2014 October 19. If an electron temperature of 10 eV (not shown) is considered, the RPC-LAP density is still above the density derived from the ionospheric model driven by solar photoionization alone, except between 09 and 10 UT during which RPC-LAP electron density overlaps with the top boundary of the modelled density. It reaches around 180 cm^{-3} at 08:30 UT, 14:00 UT and 18:00 UT, a factor up to 3 from the top boundary of the density from the photoionization model. Furthermore, several features in RPC-LAP are not present in the ROSINA-COPS neutral density. For instance, around 08:30–09:00 UT (just after the RPC-LAP data gap), the large

drop in RPC-LAP electron density cannot be explained by the modest decrease in n_n . In addition, while the neutral density is constant, the RPC-LAP electron density exhibits a sharp increase at 18 UT and a sharp decrease at 21 UT. All these features are however captured by the ionospheric model when the contribution by energetic electrons is included.

Before 06 UT on 2014 October 18, the RPC-LAP electron density peaks around 02:30 UT. If an electron temperature of 7.5 eV is assumed, the contribution from electron-impact ionization is required to explain the RPC-LAP electron density. However, if an electron temperature of 10 eV is assumed (not shown), the RPC-LAP electron density values are reduced and fit the density derived from the ionospheric model driven by solar photoionization alone. Though an electron temperature of 7.5 eV seems more suitable based on RPC-LAP and RPC-MIP comparison on 2014 October 17 (see Section 4.1), the uncertainty in T_e renders difficult to quantify the importance of electron-impact ionization during the early morning of 2014 October 18. However, it seems most likely that their contribution is significant and needs to be included in the model to explain the observations.

5 DISCUSSION

There are several assumptions which we have made in the model and which we would like to discuss further here.

(i) The ions are assumed to move radially and not to undergo any acceleration between the surface and the spacecraft. The solar wind particles detected *in situ* by RPC-IES (see Figs 4 and 5) are reaching all the way to the cometary surface, as attested by the detection of refractory elements, such as Na, K, Si and Ca, most likely due to solar wind sputtering of dust on the surface (Wurz et al. 2015), over the Southern hemisphere – where the outgassing activity is the lowest (see Section 3.2) and we observed the most intense energetic electron flux densities (see Section 3.4.3). Moreover, at the location of *Rosetta*, the solar wind ions undergo significant deflection (Broiles et al. 2015; Nilsson et al. 2015a; Behar et al. 2016). Based on the magnetic field measurements (see Figs 4 and 5) and as expected at such large heliocentric distances for a low outgassing comet (Rubin et al. 2014; Koenders et al. 2015), there is no magnetic cavity formed in the region probed by *Rosetta*. The diamagnetic cavity was only detected closer to perihelion (Goetz et al. 2016). The newly born ions are slow compared with the solar wind plasma. They could be accelerated by the solar wind motional electric field $\mathbf{E}_{\text{sw}} = -\mathbf{u}_{\text{sw}} \times \mathbf{B}_{\text{IMF}}$ (where \mathbf{u}_{sw} is the solar wind bulk velocity) and begin to gyrate around the interplanetary magnetic field \mathbf{B}_{IMF} . For a solar wind bulk velocity magnitude of 400 km s⁻¹ and an interplanetary magnetic field B_{IMF} of the order of 1 nT assumed perpendicular to the flow, the motional electric field is 0.4 mV m⁻¹. There has been evidence of some pick-up processes with the detection of accelerated water ions by RPC-ICA (Nilsson et al. 2015a,b; Behar et al. 2016) and by RPC-IES (Broiles et al. 2015; Goldstein et al. 2015; Mandt et al. 2016). These processes affect the ion composition, in particular the H₃O⁺-to-H₂O⁺ ratio as seen near perihelion (Fuselier et al. 2016). Assuming an acceleration in the local radial direction, a newly born water ion produced close to the surface could a priori gain up to 3.4 eV at 10 km (6 km s⁻¹) and 7.4 eV (9 km s⁻¹) by 20 km (Fuselier et al. 2015). Note also that depending on the orientation of the electric field, accelerated ions could also come from upstream and have undergone larger acceleration. Nevertheless, at cometocentric distances less than 20 km:

(a) Ions produced near the surface ($r_s = 1.5$ km) take less than a minute (46 s at 400 m s⁻¹) to reach the spacecraft at 20 km distance. Considering a typical solar wind magnetic field of 1 nT at 3 au, the gyro-period of water ions is 1200 s. The propagation time from the cometary surface to *Rosetta* at 20 km is at least 25 times less than the gyro-period of water ions under a solar wind magnetic field of 1 nT (Fuselier et al. 2015). Therefore, despite the presence of a magnetic field, ions can be assumed moving radially from their source up to the spacecraft.

(b) Within the coma, the motional electric field is more accurately given by $\mathbf{E}_{\text{sw}} = -\mathbf{u} \times \mathbf{B}_{\text{IMF}}$, where the mean plasma velocity $\mathbf{u} = \frac{n_{\text{sw}}\mathbf{u}_{\text{sw}} + n_i\mathbf{u}_i}{n_{\text{sw}} + n_i}$. As *Rosetta* is in the terminator plane in 2014 October, \mathbf{u}_{sw} can be considered to be roughly perpendicular to \mathbf{u}_i .

For a solar wind number density n_{sw} of 1 cm⁻³ and a cometary ion number density n_i of 100 cm⁻³ as observed at 10–20 km, the solar wind motional electric field is reduced by a factor of 100 (assuming \mathbf{u}_i perpendicular to \mathbf{B}). This yields an energy of 0.034 eV (600 m s⁻¹) at 10 km at most and 0.073 eV (880 m s⁻¹) at 20 km. The factor applied to \mathbf{u}_i is even larger closer to the comet where cometary ion densities are higher, yielding even lower velocities at the location of *Rosetta*.

(c) The location of *Rosetta* with respect to the so-called ion exobase (Lemaire & Scherer 1974) has been assessed. On the one hand, the mean free path of the ions is given by

$$\lambda_i = \frac{1}{n_n(r) \sigma_{n,i}}, \quad (17)$$

where $\sigma_{n,i}$ is the ion–neutral collision cross-section of at least 4×10^{-14} cm² (Fleshman et al. 2012). On the other hand, the total ion density scaleheight H_{n_i} is given by

$$\frac{1}{H_{n_i}} = -\frac{1}{n_i(r)} \frac{dn_i(r)}{dr} = \frac{2}{r} - \frac{1}{r - r_s} \approx \frac{1}{r} \quad (18)$$

based on equation (12). $H_{n_i} \approx r$ is consistent with the RPC-LAP observations (Edberg et al. 2015). Moreover, assuming u_i independent of r , the advection scaleheight H_{adv_i} for the total ion population is defined as

$$\frac{1}{H_{\text{adv}_i}} = \frac{1}{r^2 n_i(r) u_i} \frac{d}{dr} (r^2 n_i(r) u_i) = -\frac{1}{H_{n_i}} + \frac{1}{H_g}, \quad (19)$$

where H_g is the geometric scaleheight, given by

$$\frac{1}{H_g} = \frac{1}{r^2} \frac{d}{dr} (r^2) = \frac{2}{r}. \quad (20)$$

Thus, $H_{\text{adv}_i} = r - r_s = H_{n_i} \approx r$. Note that $H_{n_i} = u_i \tau_{n_i}$ and $H_g = u_i \tau_g$, where the time-scales τ are defined in Section 2.

The mean free path λ_i equals the ion density scaleheight H_{n_i} (or the advection scaleheight H_{adv_i}) at a cometocentric distance r_e given by

$$r_e - r_s = \frac{1}{n_n(r_e) \sigma_{n,i}} = \frac{r_e^2}{n_n(r_0) r_0^2 \sigma_{n,i}} \quad (21)$$

that is,

$$r_e \approx n_n(r_0) r_0^2 \sigma_{n,i}. \quad (22)$$

Solving equation (21), at $r_0 = 20$ km (10 km), the number density observed is mostly above 1.5×10^7 cm⁻³ (3×10^7 cm⁻³) (see Figs 4 and 5), which yields $r_e = 22$ km (10 km). The region probed by *Rosetta* in the present study can therefore be considered close to or below the ion exobase, where ions are (nearly) thermalized. The effect of the convection electric field on particles from this region is limited and can be neglected. In addition, the accelerated

ions detected by RPC-ICA seem to come from a different direction than the cold plasma and contribute little to the total plasma density (Nilsson et al. 2015a,b). It is justified to ignore them here. Regarding electrons, the bulk has energies in the 7–10 eV range and cross-section with H₂O of the order of 10^{-17} – 10^{-16} cm² (Itikawa & Mason 2005). An ambipolar electric field is anticipated to build up in order to prevent them to escape too fast and to ensure charge neutrality.

(ii) The neutral number density follows an r^{-2} law. Though observations from ROSINA-COPS are consistent with an r^{-2} dependence (Bieler et al. 2015b; Hässig et al. 2015), the non-spherical shape may lead to a deviation from the r^{-2} law. The ROSINA measurements have been obtained from cometocentric distances near 10 km and beyond. Close to the surface, the neutral number density may depart from the r^{-2} law and increase more substantially as r decreases. Based on an exospheric model of Mercury adapted to comet 67P conditions (Wurz et al. 2010a,b), the neutral density profile for a surface (sublimation) temperature of about 200 K – temperature consistent with observations (Capaccioni et al. 2015) – is given by

$$n_n(r) = n_n(r_s) \left(\frac{r_s}{r} \right)^2 \left(1 + \frac{a}{r-b} \right), \quad (23)$$

where the cometocentric distance r and the radius of the assumed sphere r_s are in km, the number density n_n in cm⁻³ and the parameters $a = 0.31791$ km and $b = 1.8134$ km. Here r_s is set to 2 km, while in the rest of the paper it is set to 1.5 km. Our default profile defined by equation (6) is obtained assuming parameter $a = 0$. The density $n_n(r_s)$ is derived by applying equation (23) at $r = r_0$, which gives

$$n_n(r_s) = n_n(r_0) \left(\frac{r_0}{r_s} \right)^2 \left(\frac{r_0 - b}{r_0 - b + a} \right). \quad (24)$$

Being given a number density $n_n(r_0)$ at the location of *Rosetta*, the density profile defined by equation (23) and the default one in r^{-2} are nearly identical down to about 3 km. At the surface, the former has a density value a factor of 2.6 higher than the default one. In terms of the ionospheric density, this yields large differences very close to the surface, but at 4 km (10 km, 20 km), the difference in ionospheric density is of 35 per cent (10 per cent, 4 per cent). Note that for the default neutral density profile in r^{-2} , assuming r_s of 2 km, instead of 1.5 km, yields a decrease of 6 per cent (3 per cent) in n_i at 10 km (20 km).

(iii) The neutral outflow velocity is assumed to be independent of r . Monte Carlo modelling has shown that when the gas leaves the surface, its outflow velocity undergoes a rapid, monotonic increase in the first metres to km, followed by a slow asymptotic approach to the terminal, expansion value (Davidsson et al. 2010). Lower values of u_n closer to the surface mean higher number density as well as higher values of the ionospheric densities. As discussed in point (ii) just above about n_n , the increase in the neutral density has a limited effect on the ionospheric densities at the location of *Rosetta*. Moreover, taking RPC-MIP as a reference, the agreement between the modelled and the observed electron density implies that no significant departure of u_n away from the range of values considered here seems to be occurring.

(iv) The effective electron-impact ionization frequency ν^e is assumed to be independent of r . This means that no substantial degradation in energy of the hot electron population and change in electron flux are assumed to occur between the surface and the spacecraft. Over the northern, summer hemisphere with a low to

medium RPC-IES electron level and medium to high outgassing activity (2014 October 03–04 and 2014 October 17), the model driven by solar photoionization alone matches well the RPC-MIP electron density measurements, while the model including electron-impact ionization overestimates the observed electron density (within the range of neutral outflow velocity values assumed). In that case, the electron-impact contribution to ionization is largely overestimated in the model and does not appear to contribute significantly to the observed electron density. Closer to the comet where neutral density becomes higher, significant energy degradation is expected to occur, similar to, though stronger than, what is seen in period T1 (see Fig. 9). Assuming a constant ionization frequency and a neutral density as in equation (6), the integral of the ionization rate between the surface r_s and a cometocentric distance r is given by

$$\int_{r_s}^r P_i(r') dr' = P_i(r_0) \int_{r_s}^r \left(\frac{r_0}{r'} \right)^2 dr' = P_i(r_0) r_0^2 \left(\frac{r - r_s}{r_s r} \right). \quad (25)$$

This implies that a percentage ζ of the total ionization, which takes place between the surface ($r_s = 1.5$ km) and *Rosetta* at r_0 , occurs between r_s and r given by $r = \frac{r_s r_0}{(1-\zeta)r_0 + \zeta r_s}$. For *Rosetta* at $r_0 = 10$ km (20 km), 75 per cent of the ionization occurs between the surface and 4.1 km (4.9 km). The neutral number density is a factor of 6 higher at r than at *Rosetta* for $r_0 = 10$ km and a factor of 17 for $r_0 = 20$ km. This corresponds to neutral density values higher than the density at the period T1 peak. Significant energy degradation may be occurring at r and the inferred electron-impact frequency is expected to be reduced. Over the winter hemisphere (from October 18 afternoon to October 19 morning), the reduction of ν^e is also anticipated, though not as high as over the Northern hemisphere. Over this region, the activity parameter is of the order of $\xi = 7.7 \times 10^{19}$ cm⁻¹ (or less), which implies a number density at 4.1 km of 4.6×10^9 cm⁻³, higher than the neutral density at the period T1 peak. However, the activity parameter over the Southern hemisphere is at least a factor of 4 less than on 2014 October 17, so the departure of $\nu^e(r)$ from $\nu^e(r_0)$ over the winter hemisphere, compared with the summer hemisphere, is expected to be more moderate. The attenuation is also moderated by secondary ionization. Unlike the steep spectra seen over the summer hemisphere, the spectra seen over the winter hemisphere are less steep and have significant energy flux density towards higher energies (see Fig. 9). This is consistent with the summer–winter hemispheric differences seen in the detection of refractory elements and attesting of the penetration of solar wind particles all the way to the surface over the Southern hemisphere (Wurz et al. 2015). This means that closer to the comet secondary ionization may occur and contribute to the electron-impact ionization.

Note that the coma in 2014 October is optically thin to solar EUV radiation, so unlike in dense planetary atmospheres, the photoelectron population is not going to become more energetic closer to the surface. In addition, the duration the neutral gas spends in the shadow cast by the comet itself is limited (self-shadowing).

6 CONCLUSION

We have shown the following.

(i) *Close to the comet* ($r < 20$ km) and at a large heliocentric distance ($d_h = 3.2$ au), cometary ions are still below the ion exobase and undergo no significant effect from the solar wind and the outgassing rate is low enough to neglect chemical loss of the plasma. Therefore, a simple balance between ionization rate of the major

neutrals and advection associated with the gas outflow velocity is sufficient to calculate the ionospheric density, as illustrated in Fig. 2. This results in an r^{-1} dependence of the ionospheric density, which is consistent with the differences in plasma density observed at 10 and 20 km (see Section 4.1) as well as earlier findings based on the analysis of RPC-LAP electron density (Edberg et al. 2015). We also demonstrated that the main sources of ionization are photoionization by solar EUV radiation and electron-impact ionization.

(ii) *Over the northern, summer hemisphere* (2014 October 03–04 and 2014 October 17) – region of high neutral density and low to medium energetic electron flux density, the solar EUV radiation is driving the ionization (see Section 4.2.1). The observed electron density can be explained by photoionization alone when taking the uncertainties in outflow velocity into account. Similar findings were recently found by Vigren et al. (2016) in a pure water gas at $r = 30$ km in 2015 January. The good agreement between RPC-MIP and modelled ionospheric density seems to imply the limited effect, at least in terms of electron density reduction, on RPC-MIP measurements, of the cloud sheet around the spacecraft. In contrast, in the morning of 2014 October 20, the local energetic electron flux density measured by RPC-IES is large compared to the 2014 October 17 level and electron-impact ionization needs to be included besides photoionization in order to explain the observed electron density.

(iii) *Over the southern, winter hemisphere* (2014 October 18–19) – region of low neutral density and intense energetic electron flux density, solar photoionization alone cannot explain the observed electron density, even when a change in composition and a large range of neutral outflow velocities ($400\text{--}700\text{ m s}^{-1}$) are taken into account. It is necessary to take electron impact into account (see Section 4.2.2). Some features seen in the electron density, such as sharp extrema, are not present in the ROSINA-COPS neutral density, but are captured when including the contribution from energetic electrons into the ionospheric model. The seasonal difference in ionization source may result from the low neutral densities over the winter hemisphere which facilitates high flux densities of electrons to reach this region. It also yields large ionospheric densities over the winter hemisphere, larger at times than in the summer hemisphere, despite the modest outgassing activity over the winter hemisphere.

(iv) *The bulk of the cometary electron population is warm.* In planetary ionospheres, the bulk of the electrons is thermal and very cold ($T_e < 0.1$ eV). The high-energy tail of the electron distribution represents the suprathermal electrons (e.g. photoelectrons, solar wind electrons, magnetospheric electrons, secondary electrons). They have enough energy to excite or ionize the neutrals as well as to heat the thermal population through Coulomb collisions. In the lowest ionospheric regions, most electrons have undergone full energy degradation by collisions with neutrals (and ions) and the ionospheric plasma is thermalized to the neutral temperature. In contrast, in the thin coma of 67P at a heliocentric distance of 3.2 au, the bulk of the electrons, seen by RPC-LAP and RPC-MIP – but hidden to RPC-IES and RPC-ICA due to the negative spacecraft potential –, remains warm (5–10 eV), as illustrated in Section 4.1 and in Odelstad et al. (2015). It has not undergone substantial energy degradation. Over the summer hemisphere, it results primarily from photoionization. It does not have enough energy to ionize, but enough to excite and dissociate the neutrals. In addition, hotter electron populations seen by RPC-IES (Clark et al. 2015; Broiles et al. 2016b), with significantly lower density, contribute to the ionization of the coma, especially over the winter hemisphere (see Section 4.2.2).

(v) *Partial energy degradation of the high-energy tail and cooling of the full electron population* were observed during periods of larger activity of ξ . For instance, a lower T_e was derived in the peaks (7.5 eV) than in the troughs (10 eV) on 2014 October 03–04; a lower T_e was also inferred over the densest gas density region analysed (period T1 on 2014 October 17). This also implies that in the EUV optically thin coma the electron-impact ionization frequency is reduced closer to the comet, though secondary ionization from the high-energy tail spectra observed at *Rosetta* over the Southern hemisphere may overcome partially the reduction.

We have also focused on two specific, extreme periods.

(i) *Period T1*, extending from 17:30 to 20:00 UT on 2014 October 17 (see Fig. 5). This region in the summer hemisphere is associated with the highest activity parameter ξ encountered in this study. With increased neutral density, the electron spectrum is strongly attenuated at high energies, which attests to energy degradation (see Fig. 9) and yields a reduction in the effective electron-impact ionization frequency (see Fig. 8). This is confirmed by the cooling inferred from the comparison of RPC-LAP with RPC-MIP: an electron temperature lower than the typical range found at other ionospheric peak times (around 7.5 eV) is required to match RPC-LAP to RPC-MIP (see Fig. 11). Furthermore, the potential ($-V_{ph}$) is not as negative as at other times when n_n is high (see Fig. 5). Though ($-V_{ph}$) is anti-correlated to n_n , it is also anti-correlated to T_e (Odelstad et al. 2015) and to the presence of a hot electron population, which are both low during T1. This would explain why ($-V_{ph}$) is not as negative as anticipated with the large n_n . Moreover, the relatively low electron density value at the 18:30 UT peak – compared with the 12:00 UT peak – may result from higher neutral outflow velocity which is expected in the most active, summer region (see Section 3.3). Finally, note that the RPC-IES electron flux could have been influenced by the rotation of the magnetic field observed during T1 around the z -axis – possibly driven by the solar wind – (see Fig. 5), which could potentially have affected the access (or escape) of energetic electrons to (from) this cometary region.

(ii) *Period T2*, extending from 18 UT on 2014 October 18 to 04 UT on 2014 October 19 (see Fig. 5). This region in the mid-latitude winter hemisphere is associated with the lowest activity parameter ξ encountered in this study. Its electron-impact ionization frequencies are the highest (see Fig. 8), associated with shallowed electron spectra of high magnitude at high energies (see Fig. 9). High fluxes for the hot electron population (see Fig. 8) may in part explain why the spacecraft potential is found to be more negative than anticipated (see Fig. 5). Furthermore, the electron-impact ionization frequency correlates with ROSINA-COPS neutral density, unlike all other periods analysed. The ionospheric density is driven by electron-impact ionization, though to quantify its contribution is limited by the uncertainty in T_e .

The origin of the hot (>10 eV) electrons detected by RPC-IES whose level increases over the low ξ activity regions of the winter hemisphere and which are driving the ionospheric densities in this region is still not fully resolved. They cannot be explained by unaffected photoelectrons or solar wind electrons. Indeed, if it would be pure photoelectrons, the energetic electrons would correlate with the activity level ξ in the summer hemisphere, which is not observed. The measured hot electrons have higher fluxes and higher energies than the solar wind population (Clark et al. 2015). Additional processes must therefore be taking place, affecting these populations. Clark et al. (2015) suggested electrostatic shock potentials, magnetic field compression and wave–particle interactions. More

recently, Broiles et al. (2016b) analysed RPC-IES and ROSINA-COPS over the Southern hemisphere on 2014 November 1. Similar to our findings during period T2, they found a positive correlation between the hot electron ($T_e > 100\,000$ K) flux density and the ROSINA-COPS neutral density. They concluded that the electron population had been heated by lower hybrid waves, though it remains unclear what population – solar wind or cometary – it is heated from. Madanian et al. (2016) also proposed the effect of ambipolar electric field with inward acceleration of electrons and, for more extreme cases, the compression of solar wind electrons associated with interplanetary shocks, as other energization processes of the electron population. The origin of the hot electrons is still under debate, but may be further constrained by the analysis of additional cases under different outgassing activities, seasons and conditions in the space environment of comet 67P.

ACKNOWLEDGEMENTS

Work at Imperial College London is supported by STFC of UK under grants ST/K001051/1 and ST/N000692/1. Work at LPC2E/CNRS was supported by CNES and by ANR under the financial agreement ANR-15-CE31-0009-01. Work on ROSINA at the University of Bern was funded by the State of Bern, the Swiss National Science Foundation and the ESA PRODEX Program. The RPC instrument package consists of five sensors (RPC-ICA, RPC-IES, RPC-LAP, RPC-MAG, RPC-MIP) and a control unit (RPC-PIU). RPC is operated by Imperial College London in cooperation with SwRI, IRF, IGEP_TU Braunschweig, IRFU, LPC2E. The lead funding agencies are CNES, SNSB, NASA, BMW and DLR, and STFC. We are indebted to the RPC and ROSINA operation and data processing teams. We are also very grateful to the TIMED/SEE PI, Tom Woods and his team for providing us with the solar flux data set, associated routines of extrapolation to planets and constructive insight on the solar data set (<http://lasp.colorado.edu/see/>). We acknowledge the staff of CDDP and Imperial College London for the use of AMDA and the RPC Quicklook data base (provided by a collaboration between the Centre de Données de la Physique des Plasmas, supported by CNRS, CNES, Observatoire de Paris and Université Paul Sabatier, Toulouse and Imperial College London, supported by the UK Science and Technology Facilities Council). Data analysis was done with the QSAS science analysis system provided by the United Kingdom Cluster Science Centre (Imperial College London and Queen Mary, University of London) supported by the Science and Technology Facilities Council (STFC).

REFERENCES

Allen M., Delitsky M., Huntress W., Yung Y., Ip W.-H., 1987, *A&A*, 187, 502
 Altwegg K. et al., 2016, *Sci. Adv.*, 2, 1600285
 Balsiger H. et al., 2007, *Space Sci. Rev.*, 128, 745
 Behar E., Nilsson H., Wieser G. S., Nemeth Z., Broiles T. W., Richter I., 2016, *Geophys. Res. Lett.*, 43, 1411
 Beth A. et al., 2016, *MNRAS*, in press
 Bieler A. et al., 2015a, *Nature*, 526, 678
 Bieler A. et al., 2015b, *A&A*, 583, A7
 Biver N. et al., 2015, *A&A*, 583, A3
 Bockelée-Morvan D. et al., 2015, *A&A*, 583, A6
 Broiles T. W. et al., 2015, *A&A*, 583, A21
 Broiles T. W. et al., 2016a, *J. Geophys. Res.: Space Phys.*, 121, 7407
 Broiles T. W. et al., 2016b, *MNRAS*, 462, S312

Burch J. L., Goldstein R., Cravens T. E., Gibson W. C., Lundin R. N., Pollock C. J., Winningham J. D., Young D. T., 2007, *Space Sci. Rev.*, 128, 697
 Burch J. L., Cravens T. E., Llera K., Goldstein R., Mokashi P., Tzou C.-Y., Broiles T., 2015, *Geophys. Res. Lett.*, 42, 5125
 Capaccioni F. et al., 2015, *Science*, 347, aaa0628
 Carr C. et al., 2007, *Space Sci. Rev.*, 128, 629
 Churyumov K. I., Gerasimenko S. I., 1972, in Chebotarev G. A., Kazimirchak-Polonskaia E. I., Marsden B. G., eds, *Proc. IAU Symp.* 45, The Motion, Evolution of Orbits, and Origin of Comets. Reidel, Dordrecht, p. 27
 Clark G. et al., 2015, *A&A*, 583, A24
 Cui J., Galand M., Coates A. J., Zhang T. L., Müller-Wodarg I. C. F., 2011, *J. Geophys. Res.*, 116, A04321
 Davidsson B. J. R., Gulkis S., Alexander C., Allmen P. v., Kamp L., Lee S., Warell J., 2010, *Icarus*, 210, 455
 Edberg N. J. T. et al., 2015, *Geophys. Res. Lett.*, 42, 4263
 Eriksson A. I. et al., 2007, *Space Sci. Rev.*, 128, 729
 Feuerbacher B., Anderegg M., Fitton B., Laude L. D., Willis R. F., Grard R. J. L., 1972, in Metzger A. E., Trombka J. I., Peterson L. E., Reedy R. C., Arnold J. R., eds, *Lunar and Planetary Science Conference Proceedings Vol. 3. Lunar and Planetary Institute, Houston*, p. 2655
 Fleshman B. L., Delamere P. A., Bagenal F., Cassidy T., 2012, *J. Geophys. Res.*, 117, E05007
 Fougere N. et al., 2016, *A&A*, 588, A134
 Fuselier S. A. et al., 2015, *A&A*, 583, A2
 Fuselier S. A. et al., 2016, *MNRAS*, 462, S67
 Génot V., Schwartz S., 2004, *Ann. Geophys.*, 22, 2073
 Glassmeier K.-H., Boehnhardt H., Koschny D., Kührt E., Richter I., 2007a, *Space Sci. Rev.*, 128, 1
 Glassmeier K.-H. et al., 2007b, *Space Sci. Rev.*, 128, 649
 Goesmann F. et al., 2015, *Science*, 349, aab0689
 Goetz C. et al., 2016, *A&A*, 588, A24
 Goldstein R. et al., 2015, *Geophys. Res. Lett.*, 42, 3093
 Granville-Phillips, 2014, *Series 370 Stabil-Ion Vacuum Measurement Controller – Instruction Manual*, 370119
 Gulkis S. et al., 2007, *Space Sci. Rev.*, 128, 561
 Gulkis S. et al., 2015, *Science*, 347, aaa0709
 Hässig M. et al., 2015, *Planet. Space Sci.*, 105, 175
 Itikawa Y., Mason N., 2005, *J. Phys. Chem. Ref. Data*, 34, 1
 Koenders C., Glassmeier K.-H., Richter I., Ranocha H., Motschmann U., 2015, *Planet. Space Sci.*, 105, 101
 Le Roy L. et al., 2015, *A&A*, 583, A1
 Lee S. et al., 2015, *A&A*, 583, A5
 Lemaire J., Scherer M., 1974, *Space Sci. Rev.*, 15, 591
 Luspay-Kuti A. et al., 2015, *A&A*, 583, A4
 Madanian H. et al., 2016, *J. Geophys. Res.: Space Phys.*, 121, 5815
 Mall U. et al., 2016, *ApJ*, 819, 126
 Mandt K. E. et al., 2016, *MNRAS*, 462, S9
 Mohammadzadeh A. et al., 2003, *IEEE Trans. Nucl. Sci.*, 50, 2272
 Nilsson H. et al., 2007, *Space Sci. Rev.*, 128, 671
 Nilsson H. et al., 2015a, *Science*, 347, aaa0571
 Nilsson H. et al., 2015b, *A&A*, 583, A20
 Odelstad E. et al., 2015, *Geophys. Res. Lett.*, 42, 10126
 Odelstad E., Stenberg-Wieser G., Wieser M., Eriksson A. I., Nilsson H., Johansson F. L., 2016, *Proc. 14th Spacecraft Charging Technology Conference. ESA, Noordwijk*, p. 123
 Rubin M. et al., 2014, *Icarus*, 242, 38
 Schläppi B. et al., 2010, *J. Geophys. Res.: Space Phys.*, 115, A12313
 Shelley E. G. et al., 1987, *A&A*, 187, 304
 Sierks H. et al., 2015, *Science*, 347, aaa1044
 Trotignon J. G. et al., 2007, *Space Sci. Rev.*, 128, 713
 Vigren E., Galand M., 2013, *ApJ*, 772, 33
 Vigren E., Galand M., Lavvas P., Eriksson A. I., Wahlund J.-E., 2015a, *ApJ*, 798, 130
 Vigren E., Galand M., Eriksson A. I., Edberg N. J. T., Odelstad E., Schwartz S. J., 2015b, *ApJ*, 812, 54

- Vigren E. et al., 2016, *AJ*, 152, 59
Wedlund C. S. et al., 2016, *A&A*, 587, A154
Woods T. N. et al., 2005, *J. Geophys. Res.: Space Phys.*, 110, A01312
Wright I. P., Sheridan S., Barber S. J., Morgan G. H., Andrews D. J., Morse A. D., 2015, *Science*, 349
Wurz P., Whitby J. A., Rohner U., Martín-Fernández J. A., Lammer H., Kolb C., 2010a, *Planet. Space Sci.*, 58, 1599
Wurz P., Whitby J. A., Rohner U., Martín-Fernández J. A., Lammer H., Kolb C., 2010b, *Planet. Space Sci.*, 58, 2051
Wurz P. et al., 2015, *A&A*, 583, A22

This paper has been typeset from a \LaTeX file prepared by the author.